Monthly Notices
of the
ROYAL ASTRONOMICAL SOCIETY

Mon. Not. R. Astron. Soc. **414,** 272–288 (2011) doi:10.1111/j.1365-2966.2011.18389.x

Abundance determination of multiple star-forming regions in the H II galaxy SDSS J165712.75+321141.4

Guillermo F. Hägele,[1,2]★† Rubén García-Benito,[1,3] Enrique Pérez-Montero,[4] Ángeles I. Díaz,[1] Mónica V. Cardaci,[1,2] Verónica Firpo,[2] Elena Terlevich,[5]‡ and Roberto Terlevich[5]§

[1]*Departamento de Física Teórica, Módulo 15, Universidad Autónoma de Madrid, 28049 Madrid, Spain*
[2]*Facultad de Cs. Astronómicas y Geofísicas, Universidad Nacional de La Plata, Paseo del Bosque s/n, 1900 La Plata, Argentina*
[3]*Kavli Institute of Astronomy and Astrophysics, Peking University, 100871 Beijing, China*
[4]*Instituto de Astrofísica de Andalucía, CSIC, Apdo. 3004, 18080 Granada, Spain*
[5] *Instituto Nacional de Astrofísica, Óptica y Electrónica, Tonantzintla, Apdo. Postal 51, 72000 Puebla, México*

Accepted 2011 January 19. Received 2011 January 19; in original form 2010 November 30

ABSTRACT

We analyse high signal-to-noise ratio spectrophotometric observations acquired simultaneously with TWIN, a double-arm spectrograph, from 3400 to 10 400 Å of three star-forming regions in the H II galaxy SDSS J165712.75+321141.4. We have measured four line temperatures – T_e([O III]), T_e([S III]), T_e([O II]) and T_e([S II]) – with high-precision, rms errors of the order of 2, 5, 6 and 6 per cent, respectively, for the brightest region, and slightly worse for the other two. The temperature measurements allowed the direct derivation of ionic abundances of oxygen, sulphur, nitrogen, neon and argon.

We have computed CLOUDY tailor-made models which reproduce the O^{2+}-measured thermal and ionic structures within the errors in the three knots, with deviations of only 0.1 dex in the case of O^+ and S^{2+} ionic abundances. In the case of the electron temperature and the ionic abundances of S^+/H^+, we find major discrepancies which could be the consequence of the presence of colder diffuse gas. The star formation history derived using STARLIGHT shows a similar age distribution of the ionizing population among the three star-forming regions. This fact suggests a similar evolutionary history which is probably related to the process of interaction with a companion galaxy that triggered the star formation in the different regions almost at the same time. The hardness of the radiation field mapped through the use of the softness parameter η is the same within the observational errors for all three regions, implying that the equivalent effective temperatures of the radiation fields are very similar for all the studied regions of the galaxy, in spite of some small differences in the ionization state of different elements.

Regarding the kinematics of the galaxy, the gas rotation curve shows a deviation from the circular motion probably due either to an interaction process or to an expanding bubble or shell of the ionized gas approaching us. A dynamical mass of $2.5 \times 10^{10}\,M_\odot$ is derived from the rotation curve.

Key words: ISM: abundances – H II regions – galaxies: abundances – galaxies: fundamental parameters – galaxies: starburst – galaxies: stellar content.

1 INTRODUCTION

Star formation is an ongoing process in the Local Universe, with observed rates of the order of $10^{-2}\,M_\odot\,yr^{-1}\,Mpc^{-3}$ (Madau et al. 1996). Most of the light and metals are produced in the most massive among the newly formed stars. The most extreme regions forming massive stars are often referred to as starbursts. In the Local Universe, they account for about a quarter of all star formation (Heckman 1997) and this fraction may have been larger in the

★E-mail: guille.hagele@uam.es, ghagele@fcaglp.edu.ar
†Member of the Carrera de Investigador Científico, Consejo Nacional de Investigaciones Científicas y Técnicas (CONICET)
‡Visiting Astronomer at the Institute of Astronomy, University of Cambridge, Madingley Road, Cambridge CB3 0HA.
§Research Affiliate, Institute of Astronomy, University of Cambridge, Madingley Road, Cambridge CB3 0HA.

younger Universe. The origin of the term 'starburst' (coined as 'starburst nuclei' by Weedman et al. 1981) dates back to the early observations of dust-obscured star-forming regions in the centres of nearby galaxies at the end of the 1970s and beginning of the 1980s, but the basic concept extends further back (e.g. Hodge 1969; Searle, Sargent & Bagnuolo 1973).

The level of intensity of a starburst is highly variable. According to Terlevich (1997), in a starburst galaxy, the energy output of the starburst (L_{SB}) is much larger than the one coming from the rest of the galaxy (L_G); a galaxy with $L_{SB} \sim L_G$ is a galaxy with starbursts and in a normal galaxy $L_{SB} \ll L_G$. This classification shows the variety of environments of the bursts. It is clear that the visibility of the burst depends not only on its intensity but also on its environment. Terlevich (1997) also proposed a division in phases of the starburst. The first one, the nebular phase, is characterized by the presence of strong emission lines from the gas photoionized by young massive stars, with an age of less than 10 Myr. The early continuum phase goes from 10 to 100 Myr, when some Balmer lines appear in absorption and others in emission. Finally, the late continuum phase is when only some weak emission lines appear in the spectrum. The H II galaxies are typical examples of the first phase.

H II galaxies are gas-rich dwarf galaxies experiencing a violent star formation period which dominates the optical spectrum of the host galaxy. They have one of the highest intensity levels of the star-forming activity. In general, these galaxies have a central region which contains one or more star-forming knots, with a diameter of several hundred parsecs with a high surface brightness, and a low-luminosity underlying galaxy ($M_V \geq -17$). The activity of the star formation episodes cannot be sustained continuously for long periods of time, since the central region cannot have enough gas to fuel these processes for longer than 10^9 yr and to match the gas content and metallicity with theoretical considerations (Thuan, Hibbard & Lévrier 2004).

Spectroscopically, H II galaxies are essentially identical to the giant H II regions found in nearby irregular and late-type galaxies. The correlation among structural parameters (Hβ luminosity, velocity dispersion, linewidths) and between these parameters and the chemical composition (Terlevich & Melnick 1981) favours the interpretation of H II galaxies as giant H II regions in distant dwarf irregular galaxies similar to the ones found nearby (Melnick, Terlevich & Eggleton 1985).

Other important characteristic of H II galaxies is their low metallicity ($Z_\odot/50 \leq Z \leq Z_\odot/3$; Kunth & Sargent 1983). The fact that H II galaxies are metal poor and very blue objects seems to suggest that they are young. Nevertheless, there is evidence which indicates the presence of populations older than the ones in the starburst. This is seen in the behaviour of the surface brightness profile which is exponential in the external zones, or in the colour index, which turns redder in $V - R$ and $V - I$ (Telles & Terlevich 1997). IZw18 in particular was considered as the best candidate for a truly young galaxy. Early studies of the stellar population of IZw18 did not reveal any old population (Hunter & Thronson 1995). This contradicted some models which predict that during a starburst the heavy elements produced by the massive stars are ejected with high velocities into a hot phase, leaving the starburst region without immediate contribution to the enrichment of the interstellar medium (Tenorio-Tagle 1996). In this scenario, the metals observed now would have their origin in a previous star formation event and an underlying old stellar population would be expected. In fact, Garnett et al. (1997) attributed the high carbon abundance that they found in *HST* spectroscopy of IZw 18 as evidence for the presence of an old stellar population. In agreement with this result, using HST Archive data (Aloisi, Tosi & Greggio 1999) showed that stars older than 1 Gyr must be present in IZw 18. Moreover, studies of the resolved stellar population in the near-infrared with the NICMOS (Östlin 2000) also found that while the near-infrared colour–magnitude diagram was dominated by stars 10–20 Myr old, the presence of numerous asymptotic giant branch stars require an age of at least 10^8 yr. Legrand et al. (2000) modelled the relative abundance of metals in IZw 18 and concluded that, in addition to the present burst of the star formation, a low star formation rate (SFR) extended over a long period of time was necessary to account for the observed values.

In recent years, with the development of the Integral Field Unit instruments to perform 3D spectroscopy, works that require a spatial coverage to study extended galactic or extragalactic star-forming regions have been mainly focused on the use of this technique (Cairós et al. 2010; García-Benito et al. 2010; Monreal-Ibero et al. 2010; Pérez-Gallego et al. 2010; Relaño et al. 2010; Rosales-Ortega et al. 2010; Pérez-Montero et al. 2011; Sánchez et al. 2011). However, medium- or high-dispersion slit spectroscopy is a better option for spectrophotometry when the object is very compact or even extended but with few star-forming knots. This is also the case when good spatial and spectral resolution and simultaneous wide spectral coverage are required (see e.g. Hägele et al. 2006, 2007, 2008; Díaz et al. 2007; Cumming et al. 2008; Hägele 2008; Hägele et al. 2009, 2010; López-Sánchez & Esteban 2009, 2010a,b; Pérez-Montero et al. 2009; Firpo et al. 2010, 2011; López-Sánchez 2010).

In this paper, we present simultaneous blue and red long-slit observations obtained with the double-beam Cassegrain Twin Spectrograph (TWIN) at the 3.5-m telescope, Calar Alto Observatory, of the three brightest star-forming knots of the H II galaxy SDSS J165712.75+321141.4. This is part of a project to obtain a top-quality spectrophotometric data base to determine ionized gas parameters which are indispensable to critically test photoionization models and to explore discrepancies between models and observations. In Section 2, we show the details of the observations and data reduction. Section 3 presents the derived physical characteristics of the regions, including the electron temperature for four different species. Section 4 is devoted to the discussion of these results, and finally the summary and conclusions are presented in Section 5.

2 OBSERVATIONS AND DATA REDUCTION

2.1 Object selection

Using the implementation of the SDSS data base in the INAOE Virtual Observatory Superserver,[1] we selected the brightest nearby narrow-emission-line galaxies with very strong lines and large equivalent widths of Hα from the whole SDSS data release available at the time of planning the observations. These preliminary lists were then processed using BPT (Baldwin, Phillips & Terlevich 1981) diagnostic diagrams to remove active galactic nucleus like objects. The final list consisted of about 10 500 bona fide bright H II galaxies. They show spectral properties indicating a wide range of gaseous abundances and ages of the underlying stellar populations (López 2005). From this list, the final set was selected by further restricting the sample to the largest Hα flux and highest signal-to-noise ratio (S/N) objects (for a complete description of the selection criteria, see Hägele et al. 2006, hereinafter Paper I). Of the selected

[1] http://astro.inaoep.mx/en/observatories/virtual/

Table 1. Right ascension, declination, redshift and SDSS photometric magnitudes of the observed knots obtained using the SDSS explore tools.[a]

Object ID (spSpec SDSS)	Hereinafter ID	Knot	RA	Dec.	Redshift	*u*	*g*	*r*	*i*	*z*
SDSS J165712.75+321141.4	SDSS J1657	A	$16^h\,57^m\,12\overset{s}{.}75$	$32^\circ\,11'\,41\overset{''}{.}42$	0.038	17.63	17.01	17.25	17.14	17.16
(spSpec-52791-1176-591)		B	$16^h\,57^m\,12\overset{s}{.}26$	$32^\circ\,11'\,43\overset{''}{.}20$	–	20.34	19.76	20.65	20.72	20.27
		C	$16^h\,57^m\,13\overset{s}{.}58$	$32^\circ\,11'\,40\overset{''}{.}09$	–	19.28	18.75	19.52	19.40	19.17

[a]http://cas.sdss.org/astro/en/tools/explore/obj.asp

sample, we chose SDSS J165712.75+321141.4 to be observed at the allocated time. Hereinafter, for simplicity, the galaxy SDSS J165712.75+321141.4 will be termed SDSS J1657.

Some general characteristics of the knots of SDSS J1657 collected from the SDSS web page are listed in Table 1.

2.2 Observations

Blue and red spectra were obtained simultaneously using TWIN mounted on the 3.5-m telescope of the Calar Alto Observatory at the Centro Astronómico Hispano Alemán (CAHA), Spain. These observations were part of a four-night observing run in 2006 June and they were acquired under excellent seeing and photometric conditions (for details, see Hägele et al. 2008, hereinafter Paper II). The blue arm covers the wavelength range 3400–5700 Å (centred at $\lambda_c = 4550$ Å), giving a spectral dispersion of 1.09 Å pixel^{-1} ($R \simeq 4170$). On the red arm, the spectral range covers from 5800 to 10 400 Å ($\lambda_c = 8100$ Å) with a spectral dispersion of 2.42 Å pixel^{-1} ($R \simeq 3350$). The slit width was ∼1.2 arcsec. The pixel size for this set-up configuration is 0.56 arcsec for both spectral ranges. The target was observed at a paralactic angle to avoid the effects of the differential refraction in the ultraviolet. As it can be seen in Fig. 1, the three main knots of SDSS J1657 are almost perfectly aligned along

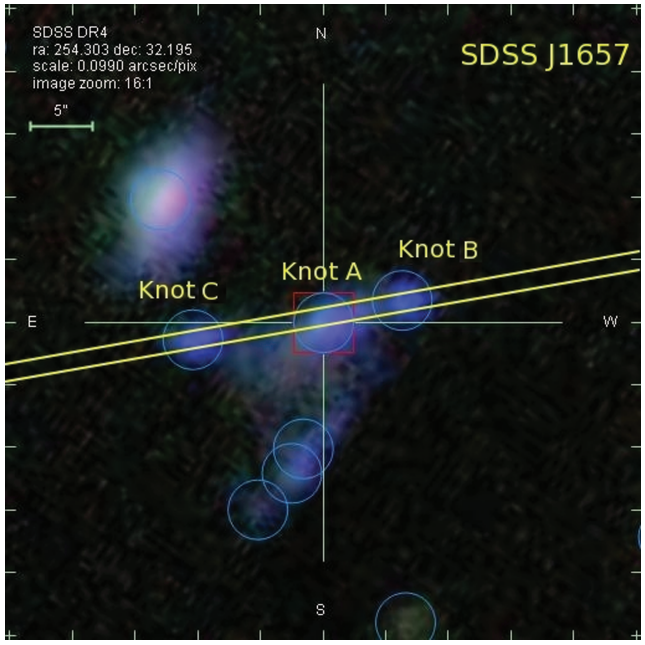

Figure 1. False-colour image of SDSS J1657 with the slit position and the adopted knot names superimposed. This image was obtained using the SDSS explore tools. The circles and squares represent the photometric and spectroscopic SDSS targets, respectively. The scale is 782 pc arcsec^{-1}, at the adopted distance for SDSS J1657. [*See the electronic edition of the Journal for a colour version of this figure.*]

Table 2. CAHA instrumental configuration.

	Spectral range (Å)	Dispersion (Å pixel^{-1})	$R_{\rm FWHM}$ [a]	Spatial resolution (arcsec pixel^{-1})
Blue	3400–5700	1.09	1420	0.56
Red	5800–10 400	2.42	1160	0.56

[a] $R_{\rm FWHM} = \lambda/\Delta\lambda_{\rm FWHM}$.

the paralactic angle. The instrumental configuration, summarized in Table 2, covers the whole spectrum from 3400 to 10 400 Å (with a gap between 5700–5800 Å) providing a moderate spectral resolution. This spectral coverage guarantees the simultaneous detection of the nebular lines from [OII] λλ 3727,29 to [SIII] λλ 9069,9532 Å at both ends of the spectrum, in the very same region of the galaxy, with a good S/N that allows the measurement of the weak auroral lines. Typical values of S/N are ∼60 for [OIII] λ 4363 and ∼20 for [SII] λ 4068 (see table 4 of Paper II).

2.3 Data reduction

Several bias and sky flat-field frames were taken at the beginning and at the end of the night in both arms. In addition, two lamp flat-fields and one He-Ar calibration lamp exposure were performed at each telescope position. The images were processed and analysed with IRAF[2] routines in the usual manner. This procedure includes the removal of cosmic rays, bias subtraction, division by a normalized flat-field and wavelength calibration. To finish, the spectra are corrected for the atmospheric extinction and flux-calibrated. Four standard star observations were performed each night at the same time for both arms, allowing a good spectrophotometric calibration with an estimated rms error of about 3 per cent. Further details concerning each of these steps can be found in Paper II.

Fig. 2 shows the spatial distribution of the Hα flux and the continuum along the slit for SDSS J1657. The emission-line profiles have been generated by collapsing 11 pixels of the spectra in the direction of the resolution at the central position of the emission lines in the rest frame, λ 6563 Å, and are plotted as a dashed line. Continuum profiles were generated by collapsing 11 resolution pixels centred at 30 Å to the red for each region and are plotted as a dot–dashed line. The difference between the two, shown as a solid line, corresponds to the pure emission. From Fig. 2, it is clear that the continuum emission is not very strong, especially in the weaker knots. The three regions are labelled in the figure. There is a weak pure emission knot located between knots A and C, which does not have enough S/N to derive the physical conditions of the gas.

[2] IRAF, the Image Reduction and Analysis Facility, is distributed by the National Optical Astronomy Observatories, which is operated by the Association of Universities for Research in Astronomy, Inc. (AURA) under cooperative agreement with the National Science Foundation (NSF).

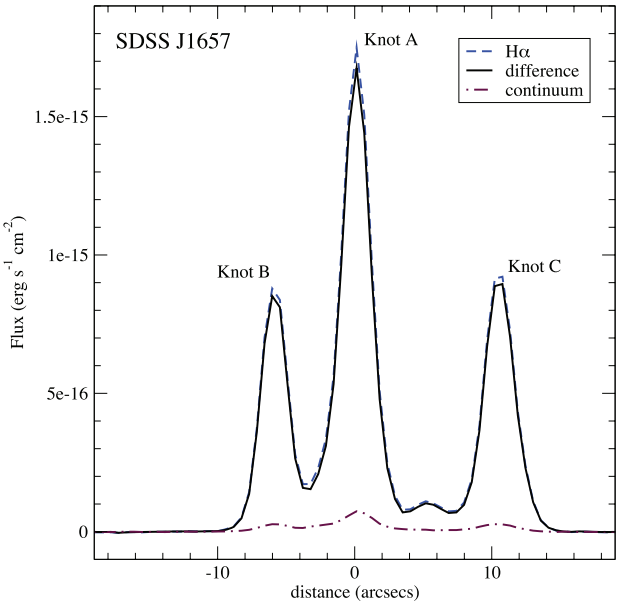

Figure 2. Spatial profile of the light distribution along the slit for the observed Hα emission. The profiles correspond to line+continuum (dashed line), continuum (dot–dashed line) and the difference between them (solid line), representing the pure emission from Hα.

3 RESULTS

3.1 Line intensities and reddening correction

The spectra of the three knots of SDSS J1657 (labelled from A to C) with some of the relevant identified emission lines are shown in Fig. 3. The spectrum of each observed knot is split into two panels. Knot A corresponds to the one analysed in Paper II.

The emission-line fluxes were measured using the splot task in IRAF following the procedure described in Paper I. Following Pérez-Montero & Díaz (2003), the statistical errors associated with the observed emission-line fluxes have been calculated using the expression

$$\sigma_1 = \sigma_c N^{1/2}[1 + \mathrm{EW}/(N\Delta)]^{1/2},$$

where σ_1 is the error in the observed line flux, σ_c represents the standard deviation in a box near the measured emission line and stands for the error in the continuum placement, N is the number of pixels used in the measurement of the line flux, EW is the line equivalent width and Δ is the wavelength dispersion in Å pixel^{-1} (González-Delgado et al. 1994). There are several emission lines affected by cosmetic faults or charge transfer in the CCD, internal reflections in the spectrograph, telluric emission lines or atmospheric absorption lines. These cause the errors to increase and, in some cases, they are impossible to quantify, in which case they were ignored and excluded from any subsequent analysis.

Some observed lines (e.g. [Cl III] λλ 5517,5537, several carbon recombination lines, Balmer or Paschen lines) were impossible to measure due to low S/N. This is also the case for the Balmer and Paschen jump that could not be measured because of the difficulty to fit the continuum at both sides of the discontinuity with an acceptable precision.

An underlying stellar population is easily appreciable by the presence of absorption features that depress the Balmer and Paschen emission lines. A pseudo-continuum has been defined at the base of the hydrogen emission lines to measure the line intensities and minimize the errors introduced by the underlying population (see Paper I). The presence of the wings of the absorption lines imply that, even though we have used a pseudo-continuum, there is still an absorbed fraction of the emitted flux that we are not able to measure accurately (see discussion in Díaz 1988). This fraction is not the same for all lines, nor are the ratios between the absorbed fractions and the emission. In Paper I, we estimated that the difference between the measurements obtained using the defined pseudo-continuum or a multi-Gaussian fit to the absorption and emission components is, for all the Balmer lines, within the errors. This is also the case for the objects studied here. At any rate, for the Balmer and Paschen emission lines, we have doubled the derived error, σ_1, as a conservative approach to include the uncertainties introduced by the presence of the underlying stellar population.

The absorption features of the underlying stellar population may also affect the helium emission lines to some extent. However, these absorption lines are narrower than those of hydrogen (see e.g. González-Delgado et al. 2005). Therefore, it is difficult to set adequate pseudo-continua at both sides of the lines to measure their fluxes.

We also applied the STARLIGHT code[3] (Cid Fernandes et al. 2005) to each region to separate the emission spectra from the underlying stellar absorptions, but for the strongest emission lines the difference between the measurements made after the subtraction of the STARLIGHT fit and the ones made using the pseudo-continuum is well below the observational errors. For a detailed discussion on the differences in the emission-line measurements, see Pérez-Montero et al. (2010).

The reddening coefficients $c(\mathrm{H}\beta)$ were calculated from the measured Balmer decrements, $F(\lambda)/F(\mathrm{H}\beta)$. We adopted the galactic extinction law of Miller & Mathews (1972) with $R_V = 3.2$. A least-squares fit of the measured decrements to the theoretical ones, $[F(\lambda)/F(\mathrm{H}\beta)]_0$, computed based on the data by Storey & Hummer (1995), was performed that provides the value of $c(\mathrm{H}\beta)$. The theoretical Balmer decrements depend on the electron density and temperature. We used an iterative method to estimate them, taking as starting values those derived from the measured [SII] λλ 6717,6731 Å and [OIII] λλλ 4363,4959,5007 Å line fluxes. Due to the large error introduced by the presence of the underlying stellar population, only the strongest Balmer emission lines (Hα, Hβ, Hγ and Hδ) were used.

For the easiness of the comparison, we have included in the following sections the results presented in Paper II for knot A. Table 3 lists the reddening-corrected emission lines for each knot, together with the reddening constant and its error taken as the uncertainties of the least-squares fit and the reddening-corrected Hβ intensity. Column 1 shows the wavelength and the name of the measured lines. The adopted reddening curve, $f(\lambda)$, normalized to Hβ, is given in column 2. The errors in the emission lines were obtained by propagating in quadrature the observational errors in the emission-line fluxes and the reddening constant uncertainties. We have not taken into account errors in the theoretical intensities since they are much lower than the observational ones.

3.2 Physical conditions of the gas

The physical conditions of the ionized gas, including the electron temperature (T_e) and electron density [$N_e \approx n([\mathrm{S\,II}])$], have been

[3] The STARLIGHT project is supported by the Brazilian agencies CNPq, CAPES and FAPESP, and by the France–Brazil CAPES/Cofecub program.

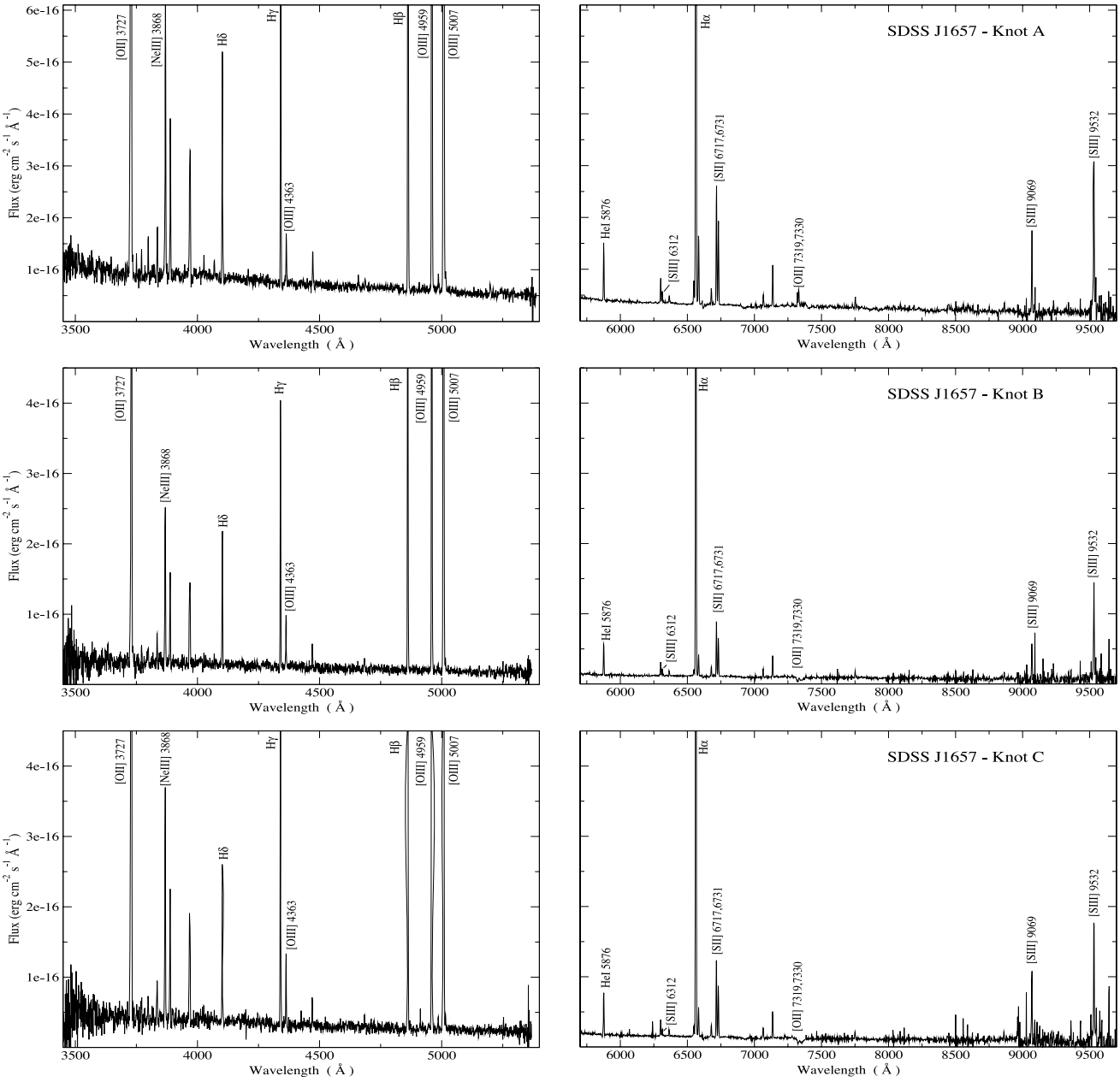

Figure 3. Blue and red spectra of knots A, B and C of SDSS J1657 (upper, middle and lower panels, respectively) in the rest frame. The flux scales are the same in both spectral ranges.

derived from the emission-line data using the same procedures as in Paper II, based on the five-level statistical equilibrium atom approximation in the task temden of the software package IRAF (de Robertis, Dufour & Hunt 1987; Shaw & Dufour 1995). As usual, we have taken as sources of error the uncertainties associated with the measurement of the emission-line fluxes and the reddening correction, and we have propagated them through our calculations.

For all three knots, we have derived the electron temperatures of [O II], [O III], [S II] and [S III]. The [O II] λλ 7319,7330 Å lines have a contribution by direct recombination which increases with the temperature. Using the calculated [O III] electron temperatures, we have estimated these contributions to be less than 4 per cent in all cases and therefore we have not corrected for this effect. The expression for the correction of the direct recombination, however, is valid only in the range of temperatures between 5000–10 000 K. The temperatures found are slightly over that range. At any rate, the relative contribution of the recombination to collisional intensities decreases rapidly with increasing temperature; therefore, for the high T_e values found in our objects, this contribution is expected to be small.

The derived electron densities and temperatures for the three star-forming regions are given in Table 4 along with their corresponding errors.

3.3 Chemical abundance derivation

We have derived the ionic chemical abundances of different species using the strongest available emission lines detected in the analysed spectra and the task ionic of the STSDAS package in IRAF, as described in Paper II.

Table 3. Relative reddening-corrected line intensities [$F(\mathrm{H}\beta) = I(\mathrm{H}\beta) = 10\,000$] for the three star-forming knots.

λ (Å)	$f(\lambda)$	Knot A			Knot B			Knot C		
		EW (Å)	$I(\lambda)$	Error (per cent)	EW (Å)	$I(\lambda)$	Error (per cent)	EW (Å)	$I(\lambda)$	Error (per cent)
3727 [O II][a]	0.271	120.1	$18\,832 \pm 230$	1.2	107.8	$13\,266 \pm 420$	3.2	112.2	$14\,809 \pm 282$	1.9
3750 H12	0.266	1.9	232 ± 47	20.2	–	–	–	–	–	–
3770 H11	0.261	2.3	293 ± 40	13.8	9.7	617 ± 146	23.7	–	–	–
3798 H10	0.254	4.1	500 ± 68	13.5	–	–	–	4.9	465 ± 141	30.4
3835 H9	0.246	7.1	780 ± 93	11.9	8.9	783 ± 180	23.0	7.5	761 ± 140	18.4
3868 [Ne III]	0.238	23.1	3262 ± 132	4.0	30.7	3663 ± 132	3.6	28.6	3533 ± 118	3.3
3889 He I+H8	0.233	14.0	1826 ± 95	5.2	22.3	1954 ± 208	10.7	26.2	2192 ± 267	12.2
3968 [Ne III]+H7	0.216	22.4	2456 ± 121	4.9	30.1	2705 ± 221	8.2	29.9	2699 ± 237	8.8
4026 [N II]+He I	0.203	1.1	155 ± 16	10.4	4.3	327 ± 105	32.1	–	–	–
4068 [S II]	0.195	1.4	198 ± 15	7.4	1.4	153 ± 36	23.7	1.2	130 ± 35	26.9
4102 Hδ	0.188	20.9	2432 ± 65	2.7	30.2	2667 ± 163	6.1	29.2	2619 ± 173	6.6
4340 Hγ	0.142	43.1	4417 ± 97	2.2	76.5	4813 ± 219	4.5	68.7	4712 ± 140	3.0
4363 [O III]	0.138	4.5	524 ± 24	4.6	8.3	846 ± 67	7.9	8.9	838 ± 59	7.0
4471 He I	0.106	4.2	443 ± 33	7.4	4.7	405 ± 44	11.0	5.3	445 ± 41	9.3
4658 [Fe III]	0.053	1.0	107 ± 16	14.9	–	–	–	–	–	–
4686 He II	0.045	1.2	126 ± 14	11.0	4.3	313 ± 68	21.9	2.1	170 ± 24	14.2
4861 Hβ	0.000	117.8	$10\,000 \pm 79$	0.8	153.3	$10\,000 \pm 178$	1.8	167.2	$10\,000 \pm 128$	1.3
4921 He I	−0.014	0.8	75 ± 14	18.6	–	–	–	–	–	–
4959 [O III]	−0.024	152.5	$14\,333 \pm 127$	0.9	218.5	$16\,118 \pm 129$	0.8	199.2	$14\,940 \pm 114$	0.8
4986 [Fe III][b]	−0.030	1.4	135 ± 28	20.5	2.4	163 ± 57	35.1	3.2	215 ± 39	18.3
5007 [O III]	−0.035	455.1	$43\,082 \pm 240$	0.6	705.5	$48\,653 \pm 256$	0.5	613.2	$44\,727 \pm 129$	0.3
5015 He I	−0.037	2.4	222 ± 23	10.1	3.2	205 ± 35	17.3	3.2	220 ± 28	12.6
5199 [N I]	−0.078	2.0	157 ± 26	16.4	–	–	–	–	–	–
5876 He I	−0.209	18.9	1116 ± 44	3.9	23.4	991 ± 29	2.9	29.0	1149 ± 47	4.1
6300 [O I]	−0.276	8.1	438 ± 16	3.7	9.6	393 ± 26	6.7	8.6	366 ± 14	3.9
6312 [S III]	−0.278	3.7	201 ± 9	4.3	4.3	175 ± 10	5.8	3.5	148 ± 10	6.4
6364 [O I]	−0.285	2.8	152 ± 18	11.8	3.6	141 ± 20	14.4	3.0	124 ± 12	10.0
6548 [N II]	−0.311	9.4	464 ± 23	5.0	5.5	216 ± 23	10.7	6.7	266 ± 14	5.4
6563 Hα	−0.313	571.3	$27\,772 \pm 153$	0.5	772.5	$28\,159 \pm 105$	0.4	730.5	$27\,919 \pm 133$	0.5
6584 [N II]	−0.316	28.8	1428 ± 47	3.3	16.2	632 ± 50	8.0	17.0	680 ± 29	4.3
6678 He I	−0.329	6.7	315 ± 18	5.7	7.3	272 ± 11	4.1	7.9	296 ± 20	6.9
6717 [S II]	−0.334	47.4	2207 ± 57	2.6	39.4	1489 ± 35	2.3	45.1	1699 ± 56	3.3
6731 [S II]	−0.336	32.2	1598 ± 43	2.7	28.1	1060 ± 25	2.3	30.7	1154 ± 40	3.4
7065 He I	−0.377	5.6	235 ± 10	4.4	7.5	226 ± 12	5.1	8.8	279 ± 26	9.3
7136 [Ar III]	−0.385	16.4	717 ± 26	3.6	18.4	584 ± 19	3.3	17.6	581 ± 17	2.9
7281 He I[c]	−0.402	0.9	41 ± 7	18.2	3.0	90 ± 14	15.9	1.4	46 ± 13	28.6
7319 [O II][d]	−0.406	12.3	302 ± 17	5.6	4.8	165 ± 15	9.2	6.1	196 ± 18	9.2
7330 [O II][e]	−0.407	8.8	211 ± 14	6.5	7.2	251 ± 21	8.4	7.9	254 ± 26	10.1
7751 [Ar III]	−0.451	4.6	177 ± 22	12.3	5.5	163 ± 13	8.0	5.8	170 ± 17	9.9
8665 P13	−0.531	7.7	144 ± 53	37.1	–	–	–	8.9	133 ± 38	28.3
8751 P12	−0.537	4.2	101 ± 29	28.2	–	–	–	–	–	–
8865 P11	−0.546	8.5	211 ± 34	16.3	17.9	277 ± 73	26.2	11.3	228 ± 46	20.2
9014 P10	−0.557	15.4	167 ± 36	21.5	–	–	–	–	–	–
9069 [S III]	−0.561	59.2	1400 ± 99	7.1	68.2	984 ± 122	12.4	81.9	1577 ± 134	8.5
9229 P9	−0.572	16.9	263 ± 47	18.0	26.1	364 ± 129	35.6	–	–	–
9532 [S III]	−0.592	157.3	3674 ± 257	7.0	85.1	2700 ± 152	5.6	238.7	2915 ± 162	5.6
I(Hβ)(erg sec^{-1} cm^{-2})			6.3×10^{-15}			2.6×10^{-15}			3.4×10^{-15}	
c(Hβ)			0.05 ± 0.01			0.15 ± 0.02			0.13 ± 0.02	

[a] [O II] λλ 3726 + 3729; [b] [Fe III] λλ 4986 + 4987; [c] possibly blend with an unknown line; [d] [O II] λλ 7318 + 7320; [e] [O II] λλ 7330 + 7331.

The total abundances have been calculated by taking into account, when required, the unseen ionization stages of each element, using the appropriate ionization correction factor (ICF) for each species, $\mathrm{X/H} = \mathrm{ICF(X^{+}}^{i}) \mathrm{X^{+}}^{i}/\mathrm{H^{+}}$ as detailed in what follows.

3.3.1 *Helium*

We have used the well-detected He I λλ 4471, 5876, 6678 and 7065 Å lines to calculate the abundances of once-ionized He. For the three knots also, the He II λ 4686 Å line was measured allowing the calculation of twice-ionized He. The He lines arise mainly from pure recombination, although they could have some contribution from the collisional excitation and be affected by the self-absorption (see Olive & Skillman 2001, 2004, for a complete treatment of these effects). We have taken the electron temperature of [O III] as representative of the zone where the He emission arises since at any rate ratios of recombination lines are weakly sensitive to the electron temperature. We have used the equations given by Olive &

Table 4. Electron densities and temperatures. Densities in cm^{-3} and temperatures in 10^4 K.

	n([S II])	T_e([O III])	T_e([O II])	T_e([S III])	T_e([S II])
Knot A	30:	1.23 ± 0.02	1.33 ± 0.07	1.45 ± 0.08	0.88 ± 0.05
Knot B	10:	1.43 ± 0.05	1.52 ± 0.12	1.64 ± 0.11	1.00 ± 0.17
Knot C	10:	1.48 ± 0.05	1.50 ± 0.13	1.29 ± 0.07	0.83 ± 0.15

Table 5. Ionic and total helium abundances.

	Knot A	Knot B	Knot C
He^+/H^+(λ4471)	0.093 ± 0.007	0.085 ± 0.009	0.094 ± 0.009
He^+/H^+(λ5876)	0.085 ± 0.003	0.079 ± 0.002	0.093 ± 0.003
He^+/H^+(λ6678)	0.086 ± 0.005	0.077 ± 0.003	0.084 ± 0.005
He^+/H^+(λ7065)	0.093 ± 0.005	0.086 ± 0.006	0.105 ± 0.010
He^+/H^+(Adopted)	0.087 ± 0.005	0.080 ± 0.005	0.092 ± 0.009
He^{2+}/H^+(λ4686)	0.0011 ± 0.0001	0.0028 ± 0.0006	0.0015 ± 0.0002
(He/H)	0.088 ± 0.008	0.080 ± 0.008	0.092 ± 0.009

Skillman to derive the He^+/H^+ value, using the theoretical emissivities scaled to Hβ from Benjamin, Skillman & Smits (1999) and the expressions for the collisional correction factors from Kingdon & Ferland (1995). To calculate the abundance of twice-ionized He, we have used equation (9) from Kunth & Sargent (1983). We have not made any corrections for the fluorescence since three of the used helium lines have a small dependence with optical depth effects but the observed objects have low densities. We have not corrected either for the presence of an underlying stellar population. A summary of the equations used to calculate these ionic abundances is given in appendix B of García-Benito (2009). The total abundance of He has been found by adding directly the two ionic abundances, $He/H = (He^+ + He^{2+})/H^+$. The results obtained for each line and the total He abundances, along with their corresponding errors, are presented in Table 5. Also given in the table is the adopted value for He^+/H^+ as the average, weighted by the errors, of the abundances derived from each He I emission line.

3.3.2 Ionic and total chemical abundances from forbidden lines

The oxygen ionic abundance ratios, O^+/H^+ and O^{2+}/H^+, have been derived from the [O II] λλ 3727,29 Å and [O III] λλ 4959, 5007 Å lines, respectively, using for each ion its corresponding temperature. At the temperatures derived here, most of the oxygen is in the form of O^+ and O^{2+}; therefore, the approximation $O/H = (O^+ + O^{2+})/H^+$ is a valid one.

S^+/H^+ and S^{2+}/H^+ abundances have been derived using T_e([S II]) and T_e([S III]), and the fluxes of the [S II] λλ 6717,6731 Å and near-infrared [S III] λλ 9069, 9532 Å emission lines, respectively. Unlike oxygen, a relatively important contribution from S^{3+} may be expected for sulphur depending on the nebular excitation. The total sulphur abundance has been calculated using an ICF for $S^+ + S^{2+}$ according to the formula by Barker (1980), which is based on Stasińska (1978) photoionization models, with $\alpha = 2.5$, which gives the best fit to the scarce observational data on S^{3+} abundances (Pérez-Montero et al. 2006). Taking this ICF as a function of the ratio O^{2+}/O instead of O^+/O reduces the propagated error for this quantity.

The ionic abundance of nitrogen, N^+/H^+, has been derived from the intensities of the [N II]λλ 6548,6584 Å lines assuming $T_e([N\,II]) \approx T_e([O\,II])$. The N/O abundance ratio has been derived under the assumption that $N/O = N^+/O^+$ and N/H was calculated as log(N/H) = log(N/O)+log(O/H).

Neon is only visible in the spectra via the [Ne III] emission line at λ3868 Å, so Ne^{2+} has been derived using this line. For this ion, we have taken the electron temperature of [O III] as representative of the high-excitation zone ($T_e([Ne\,III]) \approx T_e([O\,III])$; Peimbert & Costero 1969). Classically, the total abundance of neon has been calculated assuming that $Ne/O \approx Ne^{2+}/O^{2+}$. Izotov et al. (2004) point out that this assumption can lead to an overestimate of Ne/H in objects with low excitation, where the charge transfer between O^{2+} and H^0 becomes important. Thus, we have used the expression of this ICF given by Pérez-Montero et al. (2007). It is interesting to note, however, that, given the high excitation of the observed objects, there is no significant difference between the total neon abundance derived using this ICF and those estimated using the classic approximation.

The only available emission lines of argon in the optical spectra of ionized regions correspond to Ar^{2+} and Ar^{3+}. The abundance of Ar^{2+} has been calculated from the measured [Ar III] λ 7136 Å line, assuming that $T_e([Ar\,III]) \approx T_e([S\,III])$ (Garnett 1992). [Ar IV] was not detected in the spectra. The total abundance of Ar was hence calculated using the ICF(Ar^{2+}) derived from photoionization models by Pérez-Montero et al. (2007).

The ionic abundances with respect to the ionized hydrogen of the elements heavier than helium, ICFs, total abundances and their corresponding errors are given in Table 6.

3.4 Photoionization models of the observed regions

Detailed tailor-made photoionization models were produced in order to ascertain the main properties of the ionizing stellar population and the ionized gas. The methodology is described in Pérez-Montero et al. (2010) who study the brightest knots of the H II galaxies described in Papers I and II, including knot A in SDSS J1657. Here, we describe the models for knots B and C, and compare them with the observations and with the results obtained for knot A in Pérez-Montero et al. (2010).

We have resorted to the photoionization code CLOUDY v06.02c (Ferland et al. 1998), using the equivalent width of Hβ, after removing the underlying stellar population (i.e. the population younger than 10 Myr), the Hα luminosity and the intensities of [O II] 3727 Å, [O III] 4363 and 5007 Å, [S II] 6717 and 6731 Å, and [S III] 9069 and 9532 Å relative to Hβ.

We have used for the photoionization models the same Starburst 99 stellar libraries as in the model fitting of the stellar population, described in Section 4.4, with the metallicity closest to the value measured in the gas phase, $Z = 0.004$ (=1/5 $Z_\odot$). We assumed a constant star formation history which, according to Pérez-Montero et al., gives the best agreement for the number of ionizing photons and the EW(Hβ) corrected for underlying stellar population and dust absorption effects. A thick-shell geometry and a constant density of 100 particles per cm^3 have been set as input conditions in all the models. To fit the observed properties, the distance to the ionizing source, the filling factor, the dust-to-gas ratio and the age of the stellar cluster were left as free parameters.

One of the most important parameters in the correct modelling of ionized gas nebulae is the dust absorption factor, f_d, which gives the ratio between the number of ionizing photons emitted by the stellar cluster and the number of ionizing photons absorbed by the gas (Pérez-Montero et al. 2010). This factor must be taken into account in deriving properties of the cluster from hydrogen Balmer recombination lines. It has been obtained in the best model,

Table 6. Ionic chemical abundances derived from forbidden emission lines, ICFs and total chemical abundances for elements heavier than helium. Bold face is used for the total abundances.

	Knot A	Knot B	Knot C
$12 + \log(O^+/H^+)$	7.37 ± 0.09	7.03 ± 0.12	7.10 ± 0.12
$12 + \log(O^{2+}/H^+)$	7.87 ± 0.02	7.74 ± 0.04	7.67 ± 0.04
12 + log(O/H)	7.99 ± 0.04	7.82 ± 0.05	7.78 ± 0.06
$ICF(O^+ + O^{2+})^a$	1.07	1.06	1.06
12 + log(O/H)^a	8.02 ± 0.04	7.84 ± 0.05	7.80 ± 0.06
$12 + \log(S^+/H^+)$	6.07 ± 0.08	5.76 ± 0.19	6.02 ± 0.24
$12 + \log(S^{2+}/H^+)$	6.00 ± 0.06	5.79 ± 0.07	6.02 ± 0.07
$ICF(S^+ + S^{2+})$	1.32 ± 0.05	1.51 ± 0.10	1.38 ± 0.09
12 + log(S/H)	6.46 ± 0.07	6.25 ± 0.13	6.46 ± 0.16
log(S/O)	-1.53 ± 0.08	-1.57 ± 0.14	-1.32 ± 0.17
$ICF(S^+ + S^{2+})^a$	1.07	1.18	1.14
12 + log(S/H)^a	6.37 ± 0.07	6.15 ± 0.13	6.18 ± 0.15
log(S/O)^a	-1.65 ± 0.08	-1.69 ± 0.14	-1.42 ± 0.16
$12 + \log(N^+/H^+)$	6.15 ± 0.06	5.68 ± 0.10	5.74 ± 0.09
12 + log(N/H)	6.76 ± 0.28	6.47 ± 0.39	6.42 ± 0.39
log(N/O)	-1.23 ± 0.11	-1.35 ± 0.16	-1.36 ± 0.15
$ICF(N^+)^a$	3.39	4.90	4.27
12 + log(N/H)^a	6.68 ± 0.06	6.37 ± 0.10	6.37 ± 0.09
log(N/O)^a	-1.34 ± 0.07	-1.47 ± 0.11	-1.43 ± 0.11
$12 + \log(Ne^{2+}/H^+)$	7.22 ± 0.04	7.06 ± 0.06	7.00 ± 0.05
ICF(Ne)	1.09 ± 0.00	1.08 ± 0.00	1.08 ± 0.01
12 + log(Ne/H)	7.25 ± 0.04	7.09 ± 0.06	7.04 ± 0.05
log(Ne/O)	-0.74 ± 0.06	-0.73 ± 0.08	-0.74 ± 0.08
$ICF(Ne^{2+})^a$	1.26	1.12	1.17
12 + log(Ne/H)^a	7.32 ± 0.04	7.11 ± 0.06	7.17 ± 0.05
log(Ne/O)^a	-0.70 ± 0.05	-0.73 ± 0.08	-0.73 ± 0.08
$12 + \log(Ar^{2+}/H^+)$	5.49 ± 0.06	5.31 ± 0.06	5.49 ± 0.06
$ICF(Ar^{2+})$	1.13 ± 0.02	1.23 ± 0.06	1.16 ± 0.04
12 + log(Ar/H)	5.54 ± 0.06	5.39 ± 0.06	5.55 ± 0.06
log(Ar/O)	-2.45 ± 0.07	-2.43 ± 0.08	-2.22 ± 0.08
$ICF(Ar^{2+})^a$	1.15	1.17	1.17
12 + log(Ar/H)^a	5.55 ± 0.06	5.38 ± 0.06	5.56 ± 0.06
log(Ar/O)^a	-2.47 ± 0.07	-2.46 ± 0.08	-2.24 ± 0.08

^{a}ICFs and total abundances from photoionization models (see text).

after an iterative method to fit the observed relative emission-line intensities and the corrected EW(Hβ) and L(Hα). In Fig. 4, we show the ratio between the intensities of the most-representative observed and modelled emission lines for the three knots. Data for knot A have been taken from Pérez-Montero et al. (2010). As we can see, the agreement results are excellent for all involved [O III] lines, with a deviation smaller than 5 per cent in all three knots. In the case of the [O II] lines and [S III] 9069 Å, it is better than 10 per cent. The fitting of [S III] at 6312 Å is a bit worse, with a 20 per cent of disagreement in knots A and C, and 30 per cent in knot B. The largest discrepancy is found for the [S II] lines, from 30 per cent of disagreement up to 65 per cent in the case of 6717,6731 Å in knot B. In Table 7, we compare the observed and modelled EW(Hβ), corrected for the contribution of the underlying stellar population. We also give the number of ionizing photons and other properties predicted by the individual models, such as the age of the ionizing cluster, filling factor, ionization parameter, dust-to-gas ratio and visual extinction. Regarding knot A, all quantities have been extracted from the model in Pérez-Montero et al. (2010). As we can see, the agreement between observed and modelled values is excellent, both for the number of ionizing photons and EW(Hβ).

Table 7. Observed and model-predicted properties of the three studied regions.

		Knot A	Knot B	Knot C
Age (Myr)		7.9	5.1	4.6
Absorption factor f_d		1.621	2.082	2.422
$\log Q$(H) (s^{-1})	Observed	52.59	52.20	52.34
	Model	52.59	52.26	52.29
EW(Hβ) (Å)	Observed^a	132	153	167
	Model	127	158	164
log (filling factor)		−2.52	−2.02	−2.22
$\log U$		−2.84	−2.54	−2.62
log (dust-to-gas ratio)		−1.96	−1.97	−1.81
A_V		0.32	0.49	0.55

^{a}Corrected for the underlying stellar population.

In Fig. 5, we show a comparison between the four measured electron temperatures in each of the three knots and the values predicted by the models. As we can see, the best agreement is found for T_e([O III]). In T_e([S III]), a good agreement is found only for knot A. The model temperatures are higher for T_e([S II]) and lower for T_e([O II]) than that derived from the measured line intensities. In Fig. 6, we see the same comparison for the four respective ionic abundances. As in the case of electron temperatures, the agreement between O^{2+} abundances derived from the observations and found by the models is excellent, while in the case of O^+ and S^{2+}, only

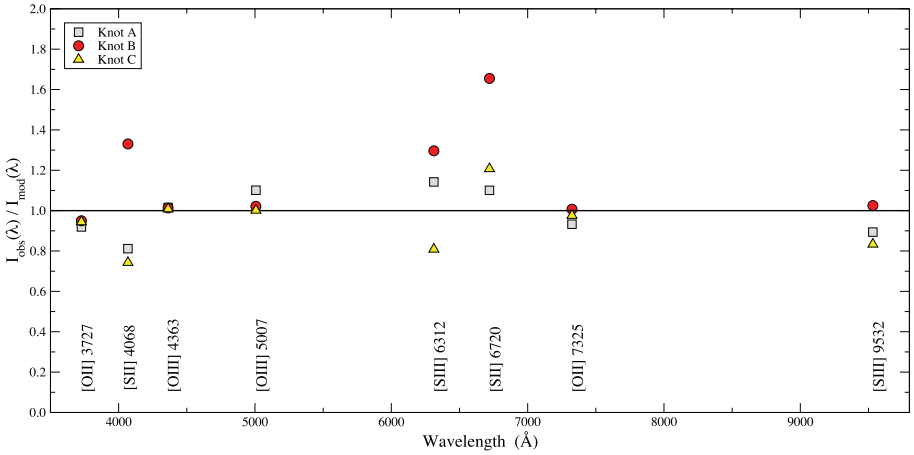

Figure 4. Ratio between observed and modelled intensities of the most-representative emission lines for each one of the star-formig knots.

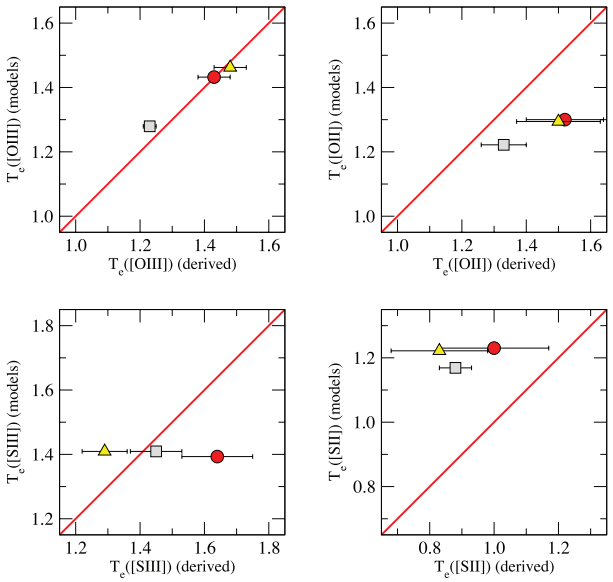

Figure 5. Measured electron temperatures for the three knots versus values predicted by the photoionization models described in the text. The symbols are: grey squares, knot A; red circles, knot B; and yellow triangles, knot C. Temperatures are in units of 10^4 K.

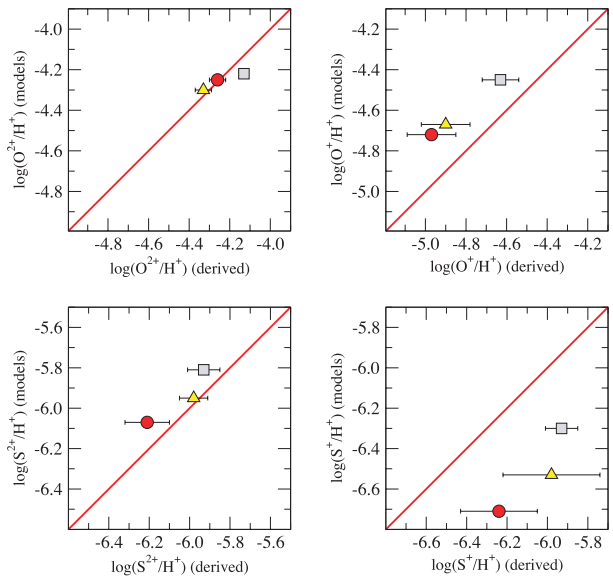

Figure 6. Modelled versus derived oxygen and sulphur ionic abundances (see description in the text). Knot A: grey squares; knot B: red circles; and knot C: yellow triangles.

deviations not larger than 0.1 dex are found. The most-evident deviation is found for the values of S^+/H^+ which are higher in the direct measurements than in the model by 0.3 dex in average for the three knots.

We have calculated the total abundances of all the measured ions, now using these models, taking into account when required the unseen ionization stages of each element, using the appropriate model-predicted ICF for each species. The predicted ICFs for O, S, N, Ar and Ne and the total abundances obtained are listed in Table 6. A discussion about the differences between the ICFs calculated by these models and those obtained from the most commonly used formulae is found in appendix A of Pérez-Montero et al. (2010).

4 DISCUSSION

4.1 Gaseous physical conditions and element abundances

4.1.1 Densities and temperatures

Four electron temperatures – T_e([O III]), T_e([O II]), T_e([S III]) and T_e([S II]) – have been estimated for the star-forming knots of SDSS J1657. The good quality of the data allows us to reach high precision, with rms errors of the order of 2, 5, 6 and 6 per cent in knot A for T_e([O III]), T_e([O II]), T_e([S III]) and T_e([S II]), respectively. For the faintest knots, knots B and C, the fractional errors are slightly higher, 3, 8, 6 and 17 per cent, respectively.

The star-forming regions show temperatures within a relatively narrow range, between 12 000–14 800 K for T_e([O III]). It is worth remembering that the adopted selection criteria for SDSS J1657 were high Hβ flux and large equivalent width of Hα, which tend to render objects with abundances and electron temperatures close to the median values shown by H II galaxies. Although these criteria applied to the main knot (the SDSS spectrum), we find similar electron temperatures for all the regions. To our knowledge, there is no previously reported T_e([O III]) for this galaxy in the literature. The estimated [O III] temperature for knot B is very similar to that of knot C; both are higher than T_e([O III]) for knot A by about 2000 K. At same the time, although differences in T_e([S III]) among the three knots are much larger, being this temperature 1900 K larger in knot B than in knot A, and 1600 K lower in knot C than in knot A, these deviations are still compatible within the errors with the empirical relation found in Paper I between T_e([O III]) and T_e([S III]) for a heterogeneous sample of giant H II regions and H II galaxies.

4.1.2 Chemical abundances

The abundances derived for the three knots using the direct method show the characteristic low values found in strong line H II galaxies (Terlevich et al. 1991; Hoyos & Díaz 2006). These values are in the range of 12+log (O/H) = 7.78–7.99, in very good agreement with what is found from the photoionization models discussed above, ranging between 7.80–8.02. The data presented in this paper are of high quality. The mean error values for the oxygen and neon abundances are 0.05 dex, 0.12 for sulphur and 0.06 for argon. Knots B and C show a similar value of 12 + log (O/H), while knot A is almost 0.2 dex higher. This difference is greater than the estimated observational errors and is similar (or even smaller) to what is found in other works with the spatial resolution of knots that belong to H II galaxies or blue compact dwarf galaxies (see e.g. Izotov et al. 1997; Vílchez & Iglesias-Páramo 1998; Kehrig et al. 2008; Cairós et al. 2009a; Pérez-Montero et al. 2009; García-Benito et al. 2010). However, in general, these differences were attributed to the observational uncertainties (pointing errors, seeing variations, etc.) or errors associated to the reddening correction and flux calibration, and the oxygen abundance variations were not assumed as statistically significant, concluding that there is a possible common chemical evolution scenario in all of them. There are even greater differences when comparing the estimated abundances of the individual knots with those derived from the integrated spectra of the galaxies. For instance, Cairós et al. (2009a) found for the integrated spectrum of Mrk 1418 a lower value of the direct oxygen abundance by about 0.35 dex (equivalent to a factor of 2.2) than for knots 1

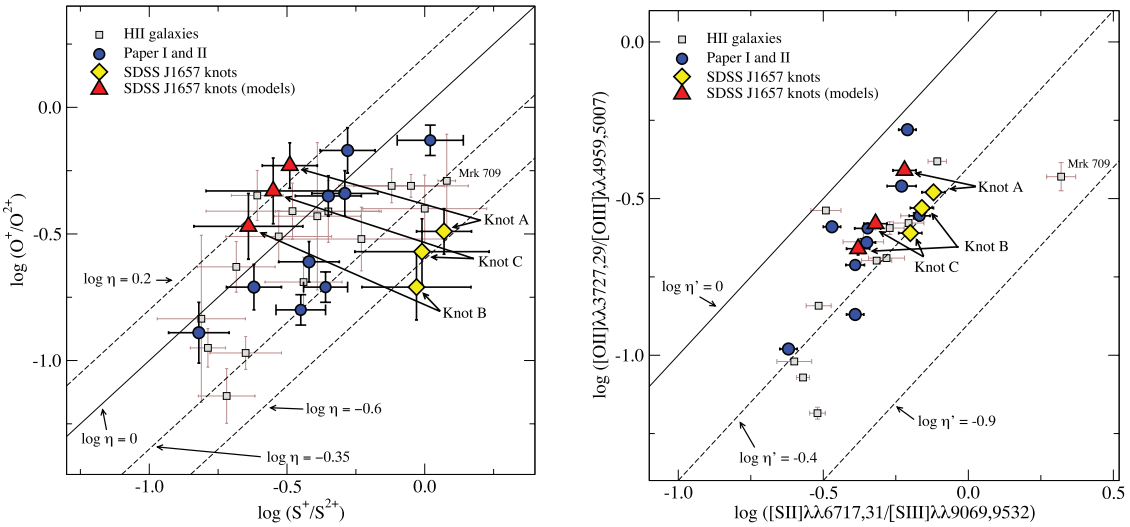

Figure 7. Left-hand panel: $\log(O^+/O^{2+})$ versus $\log(S^+/S^{2+})$ using the direct method and the photoionization models (filled yellow diamonds and red triangles), the objects studied in Papers I and II (blue circles) and H II galaxies from the literature (open squares). The diagonals in this diagram correspond to the constant values of η. Right-hand panel: log([O II]/[O III]) versus log([S II]/[S III]), symbols as in the left-hand panel. The diagonals in this diagram correspond to constant values of η'.

and 2 of that galaxy. They pointed out that while this variation could reflect a real abundance difference in different scales (kpc-sized aperture for the integrated spectrum and sizes of the order of 100 pc for individual H II regions), it may also be due to relatively large measurement uncertainties for the weak [O III] auroral emission line. Fortunately, our data are not affected by pointing errors and seeing variations, and the other observational uncertainties have a second-order effect, since TWIN is a double-beam long-slit spectrograph that simultaneously acquires all the observed spectral range. Likewise, the errors associated with the measurements of the weak auroral emission lines are relatively small, especially for [O III].

The logarithmic N/O ratios found for SDSS J1657 using the direct method are -1.23 ± 0.11, -1.35 ± 0.16 and -1.36 ± 0.15 for knots A, B and C, respectively. The derived values are on the high $\log(N/O)$ side of the distribution for this kind of objects (see the left-hand panel of fig. 6 of Paper II). The logarithmic values of this ratio found for the three knots using photoionization models are slightly lower, -1.34 ± 0.07, -1.47 ± 0.11 and -1.43 ± 0.11, respectively, although similar within the errors. However, the derived values present a larger uncertainty than the values of the total oxygen abundance, so a definite conclusion cannot be extracted about the homogeneity of this ratio. Anyway, it is quite suggestive to find a larger N/O ratio in the brightest knot, which has the larger metallicity. The N/O ratio is directly related to the chemical history of galaxies, as these two elements have different nucleosynthetic origins, so this difference can support to some extent the idea of a different chemical evolution in the three knots of this galaxy.

The $\log(S/O)$ ratios found are quite similar for knots A and B (-1.53 and -1.57, respectively) and higher for knot C (-1.32), but all three are almost equal within observational errors ($\sim$0.12 in average). The values derived using the photoionization models follow the same trend as those estimated using the direct method (-1.65, -1.69 and -1.42, respectively). They are all slightly lower than the solar value, $\log(S/O)_\odot = -1.36$ (Grevesse & Sauval 1998). On the other hand, the logarithmic Ne/O ratio is remarkably constant, with a mean value of 0.75 (0.72 from the photoionization models), despite the differences in the oxygen abundance between knot A and knots B and C. They are consistent with solar, $\log(Ne/O) = -0.61$.[4] The Ar/O ratios found (which are almost the same using the direct method and the photoionization models) show a very similar value for knots A and B, while knot C has a ratio higher by 0.2 dex. The mean value is consistent with solar, $\log(Ar/O) = -2.29$,[5] within the observational errors.

Finally, the derived helium abundances are the same for the three knots within observational errors.

4.2 Ionization structure

The ionization structure of a nebula depends essentially on the shape of the ionizing continuum and the nebular geometry and can be traced by the ratio of successive stages of the ionization of different elements. With our data it is possible to use O^+/O^{2+} and S^+/S^{2+} to probe the nebular ionization structure. In fact, Vílchez & Pagel (1988) showed that the quotient of these two quantities that they called 'softness parameter' and denoted by η is intrinsically related to the shape of the ionizing continuum and depends on the geometry only slightly. An insight into the ionization structure of the observed objects can be gained by means of the η diagram (see Paper I).

In Fig. 7 (left-hand panel), we show the relation between $\log(O^+/O^{2+})$ and $\log(S^+/S^{2+})$ derived using the direct method and the photoionization models for the knots of SDSS J1657 (filled yellow diamonds and red triangles, respectively), the objects studied in Papers I and II (blue circles) and H II galaxies (open squares) from the literature (see description and references in Paper II). In this diagram, the diagonal lines correspond to constant values of the η parameter which can be taken as an indicator of the

[4] Oxygen from Allende-Prieto, Lambert & Asplund (2001) and neon from Grevesse & Sauval (1998).

[5] Oxygen from Allende-Prieto et al. (2001) and argon from Grevesse & Sauval (1998).

ionizing temperature (Vílchez & Pagel 1988). H II galaxies occupy the region with $\log \eta$ between -0.35 and 0.2, which corresponds to high values of the ionizing temperature. As noted in Paper II, knot A shows a very low logarithmic value of η, -0.6. Knots B and C present very similar values. These objects, however, have the [O II] λλ 7319,25 Å lines affected by a set of atmospheric absorption lines. We treated the problem (as is custom) by dividing the spectra by a telluric standard. Unfortunately, no previous data of this object exist apart from the SDSS spectrum of knot A. While the agreement between the [O III] lines measured in the SDSS spectrum and ours is good, the [O II] lines measured on the SDSS spectrum provide $T_e([O\,II]) = 1.23 \pm 0.21$, lower than the one derived from our data. This lower temperature would increase the value of O^+/O^{2+}, moving the corresponding data point upwards in the left-hand panel of Fig. 7. This would be consistent with the position of the object in the right-hand panel of the figure showing log([O II]/[O III]) versus log([S II]/[S III]), which does not require explicit knowledge of the line temperatures involved in the derivation of the ionic ratios, and therefore does not depend on the method to derive or estimate these temperatures. The right-hand panel in Fig. 7 shows the purely observational counterpart of the left-hand panel. In this diagram, the diagonal lines represent constant values of $\log \eta' = \log[([O\,II]/[O\,III])/([S\,II]/[S\,III])]$.

Another possible explanation for the differences between these two diagrams can be obtained by inspecting the position of the models described above in relation to the observational points (red triangles in the figures). Models with a thick-shell geometry and a constant density predict higher $T_e([S\,II])$ and hence lower S^+/H^+, which causes the η parameter to be higher than the values estimated from the measurements. In fact, the difference between the ionic abundances derived by the direct method and those predicted by the models can be also seen in Fig. 6. On average, there is a difference of 0.23 dex for O^+/H^+, 0.07 dex for O^{2+}/H^+, 0.67 dex for S^+/H^+ and 0.13 dex for S^{2+}/H^+. This effect, already pointed out by Pérez-Montero et al. (2010), could be a consequence of an outer shell of the cold diffuse ionization structure in these objects with an extra emission of [S II] which contributes to their integrated spectrum. The agreement is better for the η' diagram, being knot B the most discrepant, which is consistent with the differences between the observed and modelled lines (see Fig. 4), where the higher difference corresponds to the [S II] lines.

In both diagrams, η and η', the three knots of SDSS J1657 present a very similar ionization structure, showing almost the same values within the observational errors. This implies that the equivalent effective temperatures of the ionization radiation field are very similar for all the knots, although we find some small differences in the ionization state of the different elements.

4.3 Chemical abundances from empirical calibrators

The emission-line spectra of the three star-forming knots in SDSS J1657 are very similar, implying similar values for the ionization parameter, ionization temperature and chemical abundances. We derived the ionization parameters from the [O II]-to-[O III] line ratio according to the expression given in Díaz et al. (2000). The logarithmic ratio is similar in all the knots ranging from -2.47 for knot B to -2.65 for knot A.

The different strong-line empirical methods for abundance derivations, which have been widely studied in the literature, are based on directly calibrating the relative intensity of some bright emission lines against the abundance of some relevant ions present in the nebula (see e.g. García-Lorenzo et al. 2008; Cairós et al. 2009b; García-Benito 2009; García-Benito et al. 2010, and references therein). For the case of oxygen, we take the calibrations studied by Pérez-Montero & Díaz (2005), who obtain different uncertainties for each parameter in a sample of ionized gaseous nebulae with accurate determinations of chemical abundances in the whole range of the metallicity.

In Fig. 8, we show the total abundances as derived from several strong-line empirical methods (with their corresponding errors

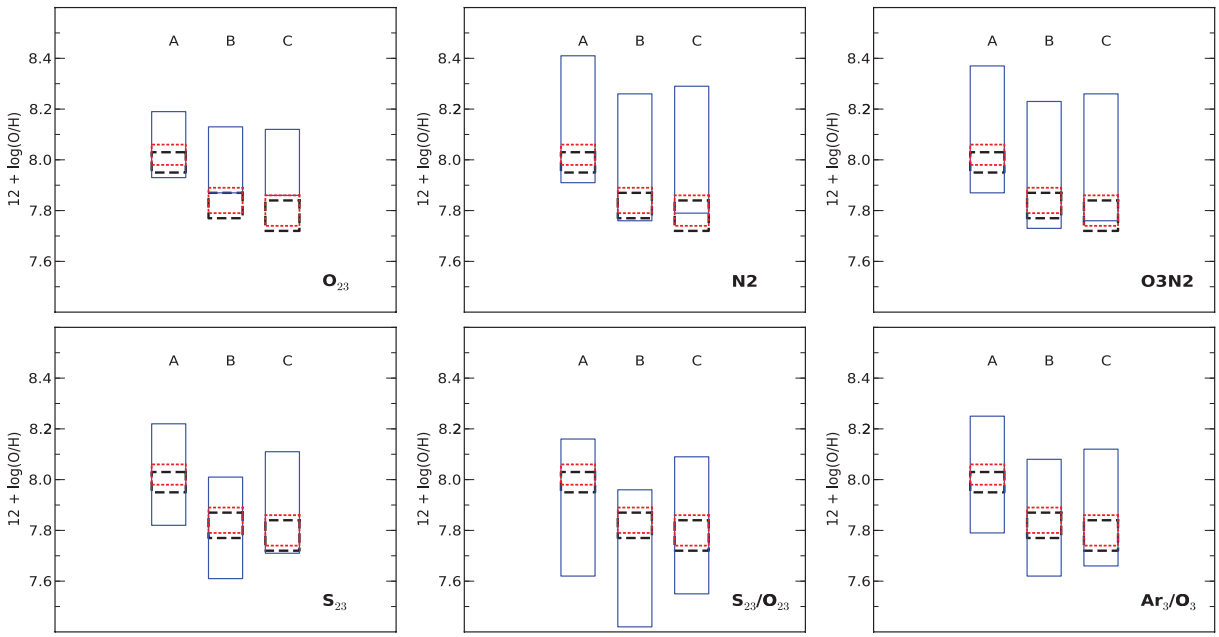

Figure 8. The oxygen abundances and their uncertainties for each observed knot of SDSS J1657 (blue solid line rectangles), as derived using different empirical calibrators. From the left-hand to right-hand panels (top): O_{23}, N2 and O3N2. For the left-hand to right-hand panels (bottom): S_{23}, S_{23}/O_{23} and Ar_3/O_3. The dashed (black) and dotted (red) line rectangles represent the abundances and their uncertainties as derived from the direct method and the photoionization models, respectively.

estimated taking into account the errors of the line intensities and also the errors given by the calibrations of the empirical parameters) and the oxygen abundances calculated from the electron temperatures measured using the direct method and those estimated from the photoionization models for each knot.

Among the available strong-line empirical parameters we studied the O_{23} parameter [also known as R_{23} and originally defined by Pagel et al. (1979) and based on [O II] and [O III] strong emission lines]. This parameter is characterized by its double-valued relation with the metallicity, with a very large dispersion in the turnover region. According to the values measured, we used the McGaugh (1991) calibration for the lower branch. For knots B and C, this calibrator fails to predict the value obtained with the direct method, overestimating the oxygen abundance, although the derived values are very similar if we take into account the observational errors and the large spread in the empirical O_{23} diagram (see fig. 3 of Pérez-Montero & Díaz 2005).

The N2 parameter (defined by Storchi-Bergmann, Calzetti & Kinney 1994) is based on the strong emission lines of [N II]. It remains single valued up to high metallicities in its relation to the oxygen abundance and it is almost independent of the reddening and flux calibrations. Nevertheless, it has the high dispersion associated to the functional parameters of the nebula (ionization parameter and ionizing radiation temperature) and to N/O variations. We used the empirical calibration of this parameter from Denicoló, Terlevich & Terlevich (2002) to derive the oxygen abundance in the three star-forming knots of this galaxy. We can see in Fig. 8 that N2 behaves similarly to O_{23} in predicting the abundances.

The parameter O3N2, defined by Alloin et al. (1979), depends on strong emission lines of [O III] and [N II]. We used the calibration due to Pettini & Pagel (2004) and, as we can see in Fig. 8, it has a very similar behaviour to that of N2.

The S_{23} parameter was defined by Vílchez & Esteban (1996) and is based on the strong emission lines of [S II] and [S III]. The calibration by Pérez-Montero & Díaz (2005) yields comparable oxygen abundances for the three observed knots that are in turn in very good agreement with the abundances derived using the direct method for knots A and B, and slightly higher for knot C, but still consistent within the errors.

The ratio of the S_{23} and O_{23} parameters, S_{23}/O_{23} (Díaz & Pérez-Montero 2000), is a parameter that increases monotonically with the oxygen abundance up to the oversolar regime and is very useful to study variations over wide ranges of metallicity (e.g. discs). We applied the calibration from Pérez-Montero & Díaz (2005) and found a good concordance with the values determined by the direct method.

The Ar_3/O_3 parameter, defined and calibrated by Stasińska (2006) as the ratio of [Ar III] λ 7136 Å to [O III] λ 5007 Å lines, predicts slightly higher values than the S_{23} parameter and in better agreement with those derived directly.

Different strong line empirical metallicity calibrators are commonly used to estimate the oxygen abundances in objects for which the direct derivation of electron temperatures is not possible. However, as illustrated in Fig. 8, different empirical calibrations give results that are not in complete agreement with direct measurements and the goodness of the result even changes between knots when using the same calibrator. Pérez-Montero et al. (2009) found a very similar behaviour for the star-forming knots of IIZw71, except for the Ar_3/O_3 parameter, which is a better estimator of the oxygen abundances for the knots in SDSS J1657. For two knots in Mrk 1418, Cairós et al. (2009a) derived the oxygen abundances from the observed [O III] λ 4363 Å auroral emission line and compared them with those abundance values derived using the N2 and O3N2 empirical parameters, and found a similar discrepancy, with the empirically derived values being slightly larger. Clearly, more observations and direct abundance estimations are needed in order to improve calibrations and truly understand the origin of the observed dispersions and discrepancies (see discussion in Paper I about the dispersion and precision of the S_{23} parameter).

4.4 The stellar population

The study of the stellar content of our objects was carried out using the STARLIGHT code, which calculates the combination of stellar libraries and the extinction law that reproduces the spectral energy distribution, to derive the properties of the stellar population in each of the knots. STARLIGHT fits an observed continuum spectral energy distribution using a combination of multiple simple stellar population (SSP; also known as instantaneous bursts) synthetic spectra using a χ^2 minimization procedure. For consistency with the photoionization models used to model the gas of knot A in Pérez-Montero et al. (2010), we have used in the fitting a synthetic stellar population obtained using STARBURST99 (Leitherer et al. 1999; Vázquez & Leitherer 2005) with the Geneva stellar evolutionary tracks for the continuous star formation with high mass-loss (Meynet et al. 1994), the Kroupa initial mass function (Kroupa 2002) in two intervals (0.1–0.5 and 0.5–100 $M_\odot$) with different exponents (1.3 and 2.3, respectively), the theoretical wind model (Leitherer, Robert & Drissen 1992), with the model atmospheres from Smith, Norris & Crowther (2002), and the stellar cluster metallicity being the closest to the nebular one, $Z = 0.004$ ($=1/5\,Z_\odot$, see Paper II and Pérez-Montero et al. 2010). The STARLIGHT code solves simultaneously the ages and relative contributions of the different SSPs and the average reddening. The reddening law from Cardelli, Clayton & Mathis (1989) is used. Prior to the fitting procedure, the spectra were shifted to the rest frame and re-sampled to a wavelength interval of 1 Å in the entire wavelength range 3500–9000 Å by interpolation the conserving flux, as required by the program. Bad pixels and emission lines were excluded from the final fits.

In Fig. 9, we show the age distribution of the visual light fraction for the individual knots. All of them present a very young stellar population with ages around 10 Myr, responsible for the ionization of the surrounding gas. Practically, all the mass of the knots seems to come from a very old population of about 8.3 Gyr. However, this result is puzzling, given that no absorption metal lines characteristic of old stellar populations, such as Mg II λ 5173 Å and/or Ca II H λ 3933 Å, Ca II K λ 3968 Å and Ca II Triplet λλ 8494, 8542, 8662 Å, are detected in the spectra. The estimated total stellar mass, the mass of the stellar population with an age younger than 10 Myr, responsible for the ionization of the gas, and the fraction of the later with respect to the former are listed in Table 8 for the three knots, together with the internal extinction, $A(V)$ (as given by STARLIGHT), and the reddening constant [$c(H\beta)$] estimated by the model. No aperture correction factors have been taken into account for the Hα luminosities, due to the compact nature of the objects. Indeed, the discrepancy factors between our Hα luminosities for knot A and those measured in the SDSS catalogue using a 3-arcsec fiber are no larger than 1.3.

We do not expect to find the same values of the extinction in the gas and the stellar population. In this galaxy, although the extinction is larger in knot A than in knots B and C (the opposite from the derived values using the Balmer decrement), the general result is consistent with low extinction.

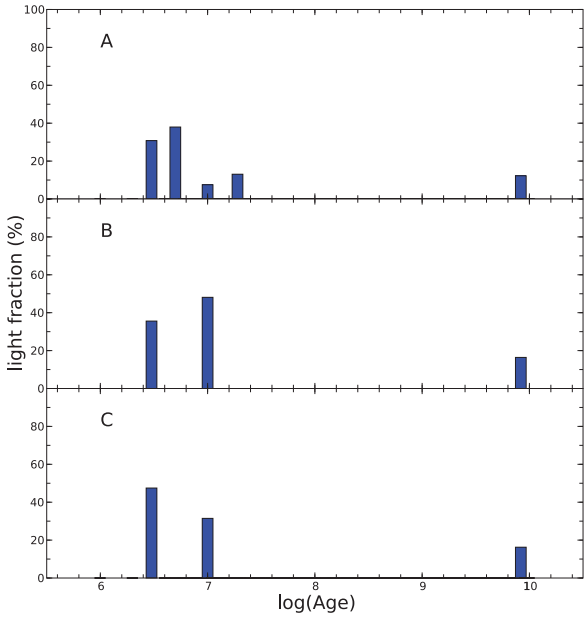

Figure 9. Histogram of the distribution in the visual light of the most-probable stellar population models fitted by STARLIGHT for knots A, B and C, as labelled.

Table 8. Values of the extinction, total stellar mass and fraction of the mass in stars younger than 10 Myr for each knot of SDSS J1657 in the best-fitting model using STARLIGHT.

ID	$A(V)$ (mag)	$c(\mathrm{H}\beta)$	M_*	$M_{\rm ion}$	$f(\mathrm{age} < 10\,\mathrm{Myr})$ (per cent)
Knot A	0.18	0.08	280	1.6	0.58
Knot B	0.00	0.00	100	0.2	0.21
Knot C	0.00	0.00	140	0.4	0.28

Note. Masses in $10^6\,\mathrm{M}_\odot$.

The mean ages and stellar mass fraction (with respect to the total stellar mass of the corresponding cluster) of the ionizing stellar population fitting by STARLIGHT for each knot are very similar, in very good agreement with the ionization structure derived in Section 4.2. Since the age distribution of the ionizing population of the different knots seems to be similar, this could indicate a common evolutionary stage of this population which is probably related to a process of interaction with a companion galaxy that triggered the star formation in different knots almost at the same time. In Fig. 1, we can appreciate a tail of the diffuse emission gas observed to the south of knot A, with a few weak and blue knots probably hosting the star formation. To the north-east, there is a bright and redder galaxy. We need more spectroscopic data to disentangle whether these different stellar systems are related or it is only a projection effect. The relatively small differences in the derived metallicities for the star-forming knots of SDSS J1657 could indicate a slightly different chemical history of these knots.

4.5 Ionizing stellar populations

Some properties of the emission knots can be obtained from the measured Hα flux, such as the Hα luminosity, the number of ionizing photons, the mass of ionizing stars and the mass of ionized hydrogen (see e.g. Díaz et al. 2000). The observed Hα flux was corrected in each knot for reddening using the values of the reddening constants, $c(\mathrm{H}\beta)$, given in Table 3. We assume a distance to SDSS J1657 of 161.2 Mpc (Mould et al. 2000). Besides, we have used the dust absorption factors, $f_{\rm d}$, derived using photoionization models to correct these quantities. These factors are independent of the reddening correction because they affect above all the number of ionizing photons emitted by the stellar cluster. As we can see in Table 7, these factors are larger in knots B and C than in knot A, consistent with the differences found in the reddening as derived by measuring the Balmer decrement. These differences in the reddening are not surprising, attending to the different ages of the ionizing clusters found in the same photoionization models (see Section 3.4), which are, respectively, 7.9, 5.1 and 4.6. Although the metallicity in knots B and C is lower, as the star formation started later in these knots, the ionizing photons have not already broken the dust cocoon usually shrouding these very young star formation knots. The derived and corrected values are given in Table 9.

Table 9. Derived properties of the observed knots using the extinction and dust absorption corrected measured Hα fluxes.

ID	$F(\mathrm{H}\alpha)$	$L(\mathrm{H}\alpha)$	$Q(\mathrm{H}_0)$	$M_{\rm ion}$	$M(\mathrm{H\,II})$	SFR
Knot A	28.4	8.3	6.3	3.6	2.1	0.697
Knot B	15.2	4.8	3.3	1.5	3.5	0.375
Knot C	23.0	7.0	5.3	2.2	5.3	0.564

Note. Fluxes in $10^{-15}\,\mathrm{erg\,s^{-1}\,cm^{-2}}$, luminosities in $10^{40}\,\mathrm{erg\,s^{-1}}$, ionizing photons in $10^{52}\,\mathrm{photon\,s^{-1}}$, masses in $10^6\,\mathrm{M}_\odot$ and SFR in $\mathrm{M}_\odot\,\mathrm{yr}^{-1}$.

The derived values of the masses of the ionizing clusters (i.e. with an age younger than 10 Myr) can be compared with those provided by the STARLIGHT fit. For knot A, STARLIGHT gives a slightly lower value than the one we derive by a factor of 2, while for knots B and C, this factor is larger, by about 7 and 5, respectively. If we take the masses derived from the Hα fluxes, which are, in principle, lower limits, since a possible escape of photons is not taken into account, and use the calculated proportions of the young to total mass given in Table 8, we obtain the total masses of about $7 \times 10^8\,\mathrm{M}_\odot$ for each knot.

The weight of the underlying stellar population in the visual light is larger in knot A than in knots B and C. The corrected EW($\mathrm{H}\beta$) is 12 per cent larger in knot A but less than 1 per cent in the other two knots.

The SFR for each knot was derived from the Hα luminosity using the expression given by Kennicutt (1998), $\mathrm{SFR} = 7.9 \times 10^{-42} \times L(\mathrm{H}\alpha)$. The derived values are also given in Table 9, taking into account dust absorption factors obtained from our models as discussed in previous sections. The SFR obtained ranges from 0.375 $\mathrm{M}_\odot\,\mathrm{yr}^{-1}$ for knot B to 0.697 $\mathrm{M}_\odot\,\mathrm{yr}^{-1}$ for knot A.

4.6 Kinematics of the knots

In Fig. 10, we show the long-slit spectrum between 5030–5220 Å (upper panel) and between 6690–7110 Å (middle panel). These spectral ranges contain Hβ and [O III] 4959,5007 Å, and Hα, [N II] 6548,6584 Å, He I 6678 Å and [S II] 6717,6731 Å emission lines, respectively. All these lines show a similar behaviour in the position–velocity (wavelength) plane, with the typical helical shape of the rotation curve expected for a rotating disc. Knot B is redshifted, while knot C is blueshifted with respect to the systemic velocity of knot A. We have analysed the differential

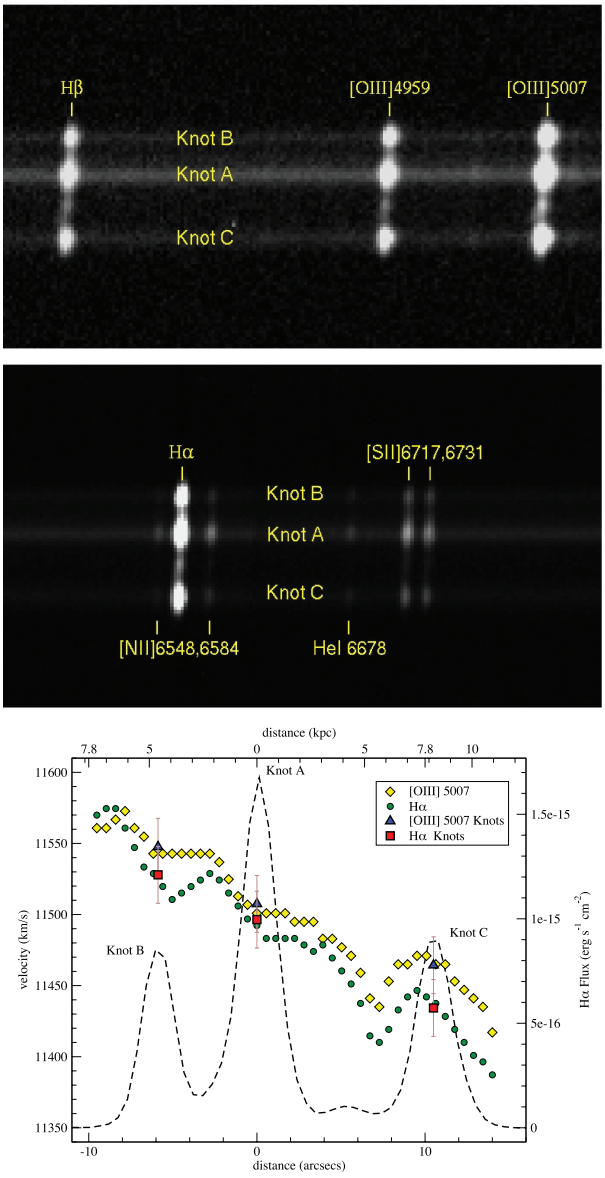

Figure 10. Long-slit spectrum between 5030–5220 Å (upper panel) and between 6690–7110 Å (middle panel); the main emission lines and the knots are labelled. The derived rotation curve of SDSS J1657 is shown in the lower panel. The green circles represent the radial velocities derived from Hα and the yellow diamonds from [O III] 5007 Å for each pixel (0.56 arcsec) along the slit. The red squares and blue upward triangles represent the radial velocities derived from Hα and [O III], respectively, using the extracted spectrum for each knot. The dashed line represents the spatial distribution of the Hα flux to be compared with the rotation curve.

radial velocity field along the slit using the Hα and [O III] emission lines. The radial velocities derived for each pixel (0.56 arcsec) are displayed in the lower panel of Fig. 10. We have also plotted the Hα spatial profile. The velocities derived from both emission lines are in good agreement, giving the same value within the observational errors, which are about 20 km s^{-1}, taking into account the errors in the wavelength calibration and a single Gaussian fitting. Larger differences ($\sim$30 km s^{-1}) between the derived velocities using the different emission lines have been found around the secondary knots, B and C, but they are also within the observational errors. From the data for knot A, we have estimated a redshift of 0.0383 ($v_r \approx 11\,500$ km s^{-1}), in very good agreement with the value given by the SDSS (see Table 1).

The rotation curve is basically linear, with some perturbations. Also the weak pure emission-line knot located between knots A and C seems to follow a circular rotation curve. There is a depression of about 50 km s^{-1} in the radial velocity curve located between this pure emission knot and knot C. In principle, we could attribute this deviation from the circular motion to a poor signal from the emission lines (see the spatial profile and the long-slit spectra, Figs 2 and 10, respectively). However, it is not the position with the lowest emission, and the other zones with low emission do not show similar deviations of the radial velocity field from the circular motion. Moreover, the radial velocities in this depression derived from the Hα and [O III] lines are in good agreement, showing a similar behaviour, which led us to assume that this depression is a real deviation from the circular motion. This could be due to the presence of an expanding bubble or shell (or superposition of more than one) of the ionized gas approaching us with respect to the systemic velocity of the galaxy defined by the velocity of the brightest and most-massive star-forming cluster, knot A. In this case, we could only see the expanding material which is moving in our direction, since we detect a systematic variation of the radial velocity, but not a broadening of the emission line with a systemic velocity in accordance with that expected for the circular motion. Another possibility would be that the ionized gas related to this weak emission area is affected by a possible interaction with a tail of the emission gas located at the south of the knots or with the redder galaxy observed to the north-east (see Fig. 1 and discussion above). This interaction could be responsible for the deviation from the circular motion as well as the fact that the ionizing population of different star-forming knots seems to have similar ages (see Section 4.4). It has been noted by Cairós et al. (2009a) that several works show that a substantial fraction of dwarf galaxies that show recent episodes of star formation have optical-faint and gas-rich low-mass companion galaxies (e.g. Taylor, Brinks & Skillman 1993; Taylor et al. 1995, 1996; Noeske et al. 2001; Pustilnik et al. 2001). Even in the case of apparent isolated galaxies, there are clues that favour the interpretation that interactions play a substantial role in the evolution of these individual systems (Bravo-Alfaro et al. 2004; Johnson et al. 2004; Östlin et al. 2004; Bravo-Alfaro, Coziol & Brinks 2006; Cumming et al. 2008; Cairós et al. 2009a).

Assuming that we see the galaxy edge-on, with a radial velocity $v_r = 100$ km s^{-1} given by the difference between knot A and the farthest point where we can measure the emission lines with a good enough S/N and considering an optical radius of 14 arcsec for this point (equivalent to $R_{opt} = 11$ Kpc at the adopted distance of 161.2 Mpc for SDSS J1657, with a scale of 782 pc arcsec^{-1}), we have estimated a dynamical mass inside this radius of 2.5×10^{10} M$_\odot$.

Since the three star-forming knots clearly dominate the luminosity of the galaxy (see Fig. 1), we have derived their blue magnitudes from the SDSS values (see Table 1). We adopt these values as a representative of the total light, although we know that they are (together) an upper limit to the total magnitude of the galaxy since we are not taking into account the light outside the 3-arcsec SDSS fibre (see Fig. 1). We have obtained the B magnitude from the Sloan g and r photometric magnitudes using the transformation equation from Chonis & Gaskell (2008), $B = g + 0.327 \times (g - r) + 0.216$, given $B_A = 17.15$, $B_B = 20.75$ and $B_C = 19.67$. We have obtained a total blue luminosity $L_B = 6.2 \times 10^9$ L$_\odot$, which gives an upper estimation of 4 for M/L_B, in agreement to what is found by Faber & Gallagher (1979) for irregular galaxies.

5 SUMMARY AND CONCLUSIONS

The star formation processes in H II galaxies are known to occur in low-density environments. Spectrophotometric observations of SDSS J1657 were carried out to study the physical properties of its individual bursts of star formation. In the three individualized star-forming regions, the electron densities were found to be well below the critical density for the collisional de-excitation.

We extracted information on the three knots of SDSS J1657, labelled A, B and C. For all of them we measured four line temperatures – T_e([O III]), T_e([S III]), T_e([O II]) and T_e([S II]) – reaching high precision with rms fractional errors of the order of 2, 5, 6 and 6 per cent, respectively, for knot A, and slightly worse, 3, 8, 6 and 17 per cent, respectively, for the fainter knots B and C. The [O III] temperature of knot A was found to be about 2000 K lower than for the other two knots. For the [O II] temperature, the estimated values for the three knots are the same within the errors. The [S III] temperatures show a difference of 3500 K between the values derived for knots B and C, and the estimated value for knot A falls in between. However, these large differences are compatible with the empirical relation between T_e([O III]) and T_e([S III]) found in Paper I, within the observational errors and the empirical dispersion of that relation. Within observational errors, the [S II] temperature derived is similar for the three knots.

The temperature measurements allowed the direct derivation of ionic abundances of oxygen, sulphur, nitrogen, neon and argon. The total abundances of these species are in the same range of metallicities measured in H II galaxies, between 7.78–7.99, with estimated errors of about 0.05 dex. Knots B and C show similar abundances, while the value for knot A is about 0.2 dex higher. This behaviour is mirrored by the N/O ratio. Knots A and B have similar Ar/O, while knot C is the one with a different value. Within observational errors, S/O is almost the same for the three knots. The Ne/O ratio is remarkably similar for all the three regions.

We have studied the underlying and ionizing stellar populations for the three regions and modelled the properties of the emitting gas using a photoionization code. The estimated electron temperatures and ionic abundances using the direct method are well reproduced by the models except for those of S^+/H^+. This could be due to the presence of diffuse gas in these star-forming regions, which is not taken into account in the models. Regarding the hardness of the radiation field, model predictions agree with observations when the softness parameter η, which parametrizes the temperature of the ionizing radiation, is expressed in terms of emission-line intensity ratios. However, there is a disagreement when ionic abundance ratios are used instead. This is probably caused by the overestimate of the electron temperature of S^+ by the models and the corresponding underestimate of the S^+/S^{2+} abundance ratio rather than by the existence of an additional heating source in these knots.

We have also estimated the total oxygen abundances by means of different strong-line empirical parameters. In all cases, the estimated abundances are consistent with those derived by the direct method with the parameter involving the sulphur lines providing the closest fit. The rest of the parameters slightly overestimate the oxygen abundance.

The star formation history for the three knots derived from the fitting of multiple SSPs using STARLIGHT is remarkably similar, with an old population of about 8 Gyr presenting more than 99 per cent contribution to the mass fraction. This result is somewhat unexpected and data on its surface brightness distribution would be very valuable to explore further this finding. Since the age distributions of the ionizing population among the different knots of SDSS J1657 seem to be similar, this could indicate a common evolutionary stage of this population which is probably related to a process of interaction with a companion galaxy that triggered the star formation in the different knots at about the same time. Besides, this interaction could be responsible for the deviation from the circular motion shown by the rotation curve, which is basically linear in the region where we can measure the emission lines with a good enough S/N. However, this deviation could be also related to an expanding bubble or shell of the ionized gas approaching us with a velocity of 50 km s^{-1} with respect to the predicted velocity from the rotation curve.

The ionization structure mapped through the use of the η and η' diagrams derived from our observations shows very similar values within the errors for all the knots. This fact implies that the equivalent effective temperatures of the ionization radiation fields are very similar for all the studied regions, in spite of some small differences in the ionization state of different elements.

Finally, we have derived a dynamical mass of 2.5×10^{10} M$_\odot$ from the rotation curve with a mean value of 100 km s^{-1} at a radius of 11 Kpc. The total mass of the young clusters derived for the three star-forming knots using the Hα luminosities is 7.3×10^6 M$_\odot$, making up a small fraction of the total dynamical mass, about 0.03 per cent. We have estimated an upper limit of about 4 for the ratio M/L_B. Data on the surface brightness distribution using broad- and narrow-band images would be very valuable to further explore this result.

ACKNOWLEDGMENTS

We acknowledge fruitful discussions with Yago Ascasibar and Amalia Meza. We also thank very much an anonymous referee for his/her careful examination of our manuscript.

We would like to thank the time-allocation committee for awarding time to this project and the support staff at Calar Alto for their cheerful and valuable assistance.

Funding for the creation and distribution of the SDSS Archive has been provided by the Alfred P. Sloan Foundation, the Participating Institutions, the National Aeronautics and Space Administration, the National Science Foundation, the US Department of Energy, the Japanese Monbukagakusho and the Max Planck Society. The SDSS website is http://www.sdss.org.

The SDSS is managed by the ARC for the Participating Institutions. The Participating Institutions are the University of Chicago, Fermilab, the Institute for Advanced Study, the Japan Participation Group, The Johns Hopkins University, the Korean Scientist Group, Los Alamos National Laboratory, the Max Planck Institute for Astronomy (MPIA), the Max Planck Institute for Astrophysics (MPA), New Mexico State University, the University of Pittsburgh, the University of Portsmouth, Princeton University, the United States Naval Observatory and the University of Washington.

This research has made use of the NASA/IPAC Extragalactic Database, which is operated by the Jet Propulsion Laboratory, California Institute of Technology, under contract with the National Aeronautics and Space Administration and of the SIMBAD, operated at CDS, Strasbourg, France.

Financial support for this work has been provided by the Spanish Ministerio de Educación y Ciencia (AYA2007-67965-C03-03 and 02). Partial support from the Comunidad de Madrid under grant S2009/ESP-1496 (ASTROMADRID) is acknowledged. EP-M also thanks to project Junta de Andalucía TIC 114. ET and RT are grateful to the Mexican Research Council (CONACYT) for support under grants CB2005-01-49847F and CB2008-01-103365. VF

would like to thank the hospitality of the Astrophysics Group of the UAM during the completion of this work.

REFERENCES

Allende Prieto C., Lambert D. L., Asplund M., 2001, ApJ, 556, L63
Alloin D., Collin-Souffrin S., Joly M., Vigroux L., 1979, A&A, 78, 200
Aloisi A., Tosi M., Greggio L., 1999, AJ, 118, 302
Baldwin J. A., Phillips M. M., Terlevich R., 1981, PASP, 93, 5
Barker T., 1980, ApJ, 240, 99
Benjamin R. A., Skillman E. D., Smits D. P., 1999, ApJ, 514, 307
Bravo-Alfaro H., Brinks E., Baker A. J., Walter F., Kunth D., 2004, AJ, 127, 264
Bravo-Alfaro H., Coziol R., Brinks E., 2006, Rev. Mex. Astron. Astrofis., 42, 261
Cairós L. M., Caon N., Zurita C., Kehrig C., Weilbacher P., Roth M., 2009a, A&A, 507, 1291
Cairós L. M., Caon N., Papaderos P., Kehrig C., Weilbacher P., Roth M. M., Zurita C., 2009b, ApJ, 707, 1676
Cairós L. M., Caon N., Zurita C., Kehrig C., Roth M., Weilbacher P., 2010, A&A, 520, A90
Cardelli J. A., Clayton G. C., Mathis J. S., 1989, ApJ, 345, 245
Chonis T. S., Gaskell C. M., 2008, AJ, 135, 264
Cid Fernandes R., Mateus A., Sodré L., Stasińska G., Gomes J. M., 2005, MNRAS, 358, 363
Cumming R. J., Fathi K., Östlin G., Marquart T., Márquez I., Masegosa J., Bergvall N., Amram P., 2008, A&A, 479, 725
de Robertis M. M., Dufour R. J., Hunt R. W., 1987, J. R. Astron. Soc. Can., 81, 195
Denicoló G., Terlevich R., Terlevich E., 2002, MNRAS, 330, 69
Díaz A. I., 1988, MNRAS, 231, 57
Díaz A. I., Pérez-Montero E., 2000, MNRAS, 312, 130
Díaz A. I., Castellanos M., Terlevich E., Luisa García-Vargas M., 2000, MNRAS, 318, 462
Díaz A. I., Terlevich E., Castellanos M., Hägele G. F., 2007, MNRAS, 382, 251
Faber S. M., Gallagher J. S., 1979, ARA&A, 17, 135
Ferland G. J., Korista K. T., Verner D. A., Ferguson J. W., Kingdon J. B., Verner E. M., 1998, PASP, 110, 761
Firpo V., Bosch G., Hägele G. F., Morrell N., 2010, MNRAS, 406, 1094
Firpo V., Bosch G., Hägele G. F., Díaz A. I., Morrell N., 2011, MNRAS, submitted
García-Benito R., 2009, PhD thesis, Universidad Autonoma de Madrid
García-Benito R. et al., 2010, MNRAS, 408, 2234
García-Lorenzo B., Cairós L. M., Caon N., Monreal Ibero A., Kehrig C., 2008, ApJ, 677, 201
Garnett D. R., 1992, AJ, 103, 1330
Garnett D. R., Skillman E. D., Dufour R. J., Shields G. A., 1997, ApJ, 481, 174
González-Delgado R. M. et al., 1994, ApJ, 437, 239
González-Delgado R. M., Cerviño M., Martins L. P., Leitherer C., Hauschildt P. H., 2005, MNRAS, 357, 945
Grevesse N., Sauval A. J., 1998, Space Sci. Rev., 85, 161
Hägele G. F., 2008, PhD thesis, Universidad Autónoma de Madrid
Hägele G. F., Pérez-Montero E., Díaz A. I., Terlevich E., Terlevich R., 2006, MNRAS, 372, 293 (Paper I)
Hägele G. F., Díaz A. I., Cardaci M. V., Terlevich E., Terlevich R., 2007, MNRAS, 378, 163
Hägele G. F., Díaz A. I., Terlevich E., Terlevich R., Pérez-Montero E., Cardaci M. V., 2008, MNRAS, 383, 209 (Paper II)
Hägele G. F., Díaz A. I., Cardaci M. V., Terlevich E., Terlevich R., 2009, MNRAS, 396, 2295
Hägele G. F., Díaz A. I., Cardaci M. V., Terlevich E., Terlevich R., 2010, MNRAS, 402, 1005
Heckman T. M., 1997, in Holt S. S., Mundy L. G., eds, AIP Conf. Ser. Vol. 393, Starbursts and Cosmogony. Am. Inst. Phys., New York, p. 271
Hodge P. W., 1969, ApJ, 156, 847
Hoyos C., Díaz A. I., 2006, MNRAS, 365, 454
Hunter D. A., Thronson H. A., Jr, 1995, ApJ, 452, 238
Izotov Y. I., Lipovetsky V. A., Chaffee F. H., Foltz C. B., Guseva N. G., Kniazev A. Y., 1997, ApJ, 476, 698
Izotov Y. I., Stasińska G., Guseva N. G., Thuan T. X., 2004, A&A, 415, 87
Johnson K. E., Indebetouw R., Watson C., Kobulnicky H. A., 2004, AJ, 128, 610
Kehrig C., Vílchez J. M., Sánchez S. F., Telles E., Pérez-Montero E., Martín-Gordón D., 2008, A&A, 477, 813
Kennicutt R. C., Jr, 1998, ARA&A, 36, 189
Kingdon J., Ferland G. J., 1995, ApJ, 442, 714
Kroupa P., 2002, Sci, 295, 82
Kunth D., Sargent W. L. W., 1983, ApJ, 273, 81
Legrand F., Kunth D., Roy J., Mas-Hesse J. M., Walsh J. R., 2000, A&A, 355, 891
Leitherer C., Robert C., Drissen L., 1992, ApJ, 401, 596
Leitherer C. et al., 1999, ApJS, 123, 3
López J., 2005, MSc Thesis, INAOE
López-Sánchez A. R., 2010, A&A, 521, A63
López-Sánchez A. R., Esteban C., 2009, A&A, 508, 615
López-Sánchez A. R., Esteban C., 2010a, A&A, 516, A104
López-Sánchez A. R., Esteban C., 2010b, A&A, 517, A85
Madau P., Ferguson H. C., Dickinson M. E., Giavalisco M., Steidel C. C., Fruchter A., 1996, MNRAS, 283, 1388
McGaugh S. S., 1991, ApJ, 380, 140
Melnick J., Terlevich R., Eggleton P. P., 1985, MNRAS, 216, 255
Meynet G., Maeder A., Schaller G., Schaerer D., Charbonnel C., 1994, A&AS, 103, 97
Miller J. S., Mathews W. G., 1972, ApJ, 172, 593
Monreal Ibero A., Vílchez J. M., Walsh J. R., Muñoz-Tuñón C., 2010, A&A, 517, A27
Mould J. R. et al., 2000, ApJ, 529, 786
Noeske K. G., Iglesias-Páramo J., Vílchez J. M., Papaderos P., Fricke K. J., 2001, A&A, 371, 806
Olive K. A., Skillman E. D., 2001, New Astron., 6, 119
Olive K. A., Skillman E. D., 2004, ApJ, 617, 29
Östlin G., 2000, ApJ, 535, L99
Östlin G., Cumming R. J., Amram P., Bergvall N., Kunth D., Márquez I., Masegosa J., Zackrisson E., 2004, A&A, 419, L43
Pagel B. E. J., Edmunds M. G., Blackwell D. E., Chun M. S., Smith G., 1979, MNRAS, 189, 95
Peimbert M., Costero R., 1969, Bol. Obs. Tonantzintla Tacubaya, 5, 3
Pérez-Gallego J. et al., 2010, MNRAS, 402, 1397
Pérez-Montero E., Díaz A. I., 2003, MNRAS, 346, 105
Pérez-Montero E., Díaz A. I., 2005, MNRAS, 361, 1063
Pérez-Montero E., Díaz A. I., Vílchez J. M., Kehrig C., 2006, A&A, 449, 193
Pérez-Montero E., Hägele G. F., Contini T., Díaz A. I., 2007, MNRAS, 381, 125
Pérez-Montero E., García-Benito R., Díaz A. I., Pérez E., Kehrig C., 2009, A&A, 497, 53
Pérez-Montero E., García-Benito R., Hägele G. F., Díaz A. I., 2010, MNRAS, 404, 2037
Pérez-Montero E. et al., 2011, A&A, submitted
Pettini M., Pagel B. E. J., 2004, MNRAS, 348, L59
Pustilnik S. A., Kniazev A. Y., Lipovetsky V. A., Ugryumov A. V., 2001, A&A, 373, 24
Relaño M., Monreal Ibero A., Vílchez J. M., Kennicutt R. C., 2010, MNRAS, 402, 1635
Rosales-Ortega F. F., Kennicutt R. C., Sánchez S. F., Díaz A. I., Pasquali A., Johnson B. D., Hao C. N., 2010, MNRAS, 405, 735
Sánchez S. F., Rosales-Ortega F. F., Kennicutt R. C., Johnson B. D., Diaz A. I., Pasquali A., Hao C. N., 2011, MNRAS, 410, 313
Searle L., Sargent W. L. W., Bagnuolo W. G., 1973, ApJ, 179, 427
Shaw R. A., Dufour R. J., 1995, PASP, 107, 896
Smith L. J., Norris R. P. F., Crowther P. A., 2002, MNRAS, 337, 1309
Stasińska G., 1978, A&A, 66, 257
Stasińska G., 2006, A&A, 454, L127

Storchi-Bergmann T., Calzetti D., Kinney A. L., 1994, ApJ, 429, 572
Storey P. J., Hummer D. G., 1995, MNRAS, 272, 41
Taylor C., Brinks E., Skillman E. D., 1993, AJ, 105, 128
Taylor C. L., Brinks E., Grashuis R. M., Skillman E. D., 1995, ApJS, 99, 427
Taylor C. L., Thomas D. L., Brinks E., Skillman E. D., 1996, ApJS, 107, 143
Telles E., Terlevich R., 1997, MNRAS, 286, 183
Tenorio-Tagle G., 1996, AJ, 111, 1641
Terlevich R., 1997, in Franco J., Terlevich R., Serrano A., eds, Rev. Mex. Astron. Astrofís. Conf. Vol. 6, 1st Guillermo Haro Conference on Astrophysics: Starburst Activity in Galaxies, p. 1
Terlevich R., Melnick J., 1981, MNRAS, 195, 839
Terlevich R., Melnick J., Masegosa J., Moles M., Copetti M. V. F., 1991, A&AS, 91, 285
Thuan T. X., Hibbard J. E., Lévrier F., 2004, AJ, 128, 617
Vázquez G. A., Leitherer C., 2005, ApJ, 621, 695
Vílchez J. M., Esteban C., 1996, MNRAS, 280, 720
Vílchez J. M., Iglesias-Páramo J., 1998, ApJ, 508, 248
Vílchez J. M., Pagel B. E. J., 1988, MNRAS, 231, 257
Weedman D. W., Feldman F. R., Balzano V. A., Ramsey L. W., Sramek R. A., Wuu C., 1981, ApJ, 248, 105

This paper has been typeset from a TEX/LATEX file prepared by the author.